We are IntechOpen, the world's leading publisher of Open Access books Built by scientists, for scientists

4,800
Open access books available

122,000
International authors and editors

135M
Downloads

Our authors are among the

154
Countries delivered to

TOP 1%
most cited scientists

12.2%
Contributors from top 500 universities

BOOK CITATION INDEX
CLARIVATE ANALYTICS
INDEXED

WEB OF SCIENCE™

Selection of our books indexed in the Book Citation Index
in Web of Science™ Core Collection (BKCI)

Interested in publishing with us?
Contact book.department@intechopen.com

Numbers displayed above are based on latest data collected.
For more information visit www.intechopen.com

Emission, Defects, and Structure of ZnO Nanocrystal Films Obtained by Electrochemical Method

Tetyana V. Torchynska and Brahim El Filali

Abstract

ZnO nanocrystal (NC) films, prepared by electrochemical etching with varying the technological routines, have been studied by means of photoluminescence (PL), scanning electronic microscopy (SEM), energy dispersion spectroscopy (EDS), Raman scattering, and X ray diffraction (XRD) techniques. Raman and XRD studies have confirmed that annealing stimulates the ZnO oxidation and crystallization with the formation of wurtzite ZnO NCs. The ZnO NC size decreases from 250–300 nm down to 40–60 nm with increasing the etching time. Two PL bands connected with the near-band edge (NBE) and defect-related emissions have been detected. Their intensity stimulation with NC size decreasing has been detected. The NBE emission enhancement is attributed to the week quantum confinement and exciton-light coupling with polariton formation in small ZnO NCs. The luminescence, morphology, and crystal structure of ZnO:Cu NCs versus Cu concentration have been investigated as well. The types of Cu-related complexes are discussed using the correlation between the PL spectrum transformations and XRD parameters. It is shown that the plasmon generation in Cu nanoparticles leads to the surface enhanced Raman scattering (SERS) effect and to PL intensity increasing the defect-related PL bands. The comparison of ZnO and ZnO:Cu NC emissions has been done and discussed.

Keywords: ZnO NCs, ZnO:Cu NCs, photoluminescence, XRD, weak quantum confinement

1. Introduction

Porous semiconductor materials stimulate the scientific interest owing to the possibility for designing the properties not known in the bulk crystals [1]. The enormous attention in the last decades has been devoted to porous silicon (PSi) that was investigated for variety

of applications in electronics, as well as for chemical, biological, and medical sensing [1]. Recently, a great interest has been shown to the ZnO nanocrystals (NCs) obtained using electrochemical technology, earlier elaborated for PSi [1–3].

The wide band gap semiconductor, such as zinc oxide, which has a direct energy band gap (3.37 eV) and a great exciton binding energy (60 meV) at 300 K, promises a lot of applications in optoelectronic devices [4–8]. Actually ZnO nanowalls and wires can be applied in white light-emitting structures [5] and UV lasers [6]. ZnO nanoneedles demonstrate the field emission characteristics [7]. Field-effect transistors on the base of ZnO nanorods were presented in Ref. [8]. ZnO nanostructures have provoked great attention recently owing to their perspectives for low voltage and short-wavelength (368 nm) electro-optical devices, as well as for protection films with high UV transparency, in different gas sensors and structures for spintronic devices [9], for a room temperature ferromagnetism, a huge magneto-optic effect, and chemical sensing [5, 9, 10].

In addition, the ZnO NC structures are interesting for phosphor applications owing to the excellent emission in orange, yellow, green, and blue ranges of PL spectra. The high concentration of radiative defects obtained in ZnO NC films permits to expect a wide spectrum of luminescence bands that is important for "white" light emitting structures [11–14]. However, the relations between the defects and structural properties of ZnO NCs (nanosheets, nanorods, etc.) are not clear yet.

For growing ZnO NCs, the following methods were used: thermal evaporation technique [15], sol-gel deposition [16], metal organic chemical vapor deposition (MOCVD) [17], molecular beam epitaxy (MBE) [18], pulse laser preparation (PLD) [19], or spray pyrolysis [20]. All mentioned methods require very expensive equipment and do not produce ZnO NCs with bright PL bands that were demonstrated recently for the electrochemical technology [21, 22]. The anodization method permits to control the ZnO NC size by varying an electrolyte content, etching times, and voltages. Additionally, this method permits simple doping of ZnO NC films by different elements.

In this chapter, ZnO and ZnO:Cu NCs were created by the electrochemical method at varying etching times or etching voltages with film annealing at high temperature (400°C) in ambient air. Photoluminescence, scanning electronic microscopy (SEM), energy dispersion spectroscopy (EDS), Raman scattering, and X-ray diffraction (XRD) have been applied for the study of ZnO and ZnO:Cu NC films.

2. ZnO NC preparation and investigations

The electrochemical anodization of Zn foils was performed in an electrolyte using two Zn electrode systems with the distance between the electrodes being 10 mm. The electrolyte was a 1:10 volume mixture of HF acid (Aldrich) and deionized water. Ultrasonic cleaning of Zn foil pieces (Aldrich 99.99%) of 6 mm radius was performed in acetone and ethanol for 15 min before etching. To investigate the impact of etching times on ZnO NC parameters, the applied

voltage was 5 V and the varied times were 1, 3, 6, and 10 min. Then ZnO films were cleaned in deionized water and annealed at 400°C for 2 h in ambient air.

To investigate the influence of voltage, the etching time was kept at 6 min and the applied voltages varied as 1, 5, 10, 15, and 20 V. Obtained ZnO films were washed in deionized water and annealed at 400°C for 2 h in ambient air.

To investigate the effect of Cu doping on the structure and optical properties of ZnO:Cu NCs, and to compare it with those in ZnO NCs, the electrochemical anodization was performed with: (i) two Zn electrodes at the creation of ZnO NCs or (ii) cathode Zn and anode Cu electrodes at the growth of ZnO:Cu NCs. Zn (Aldrich 99.99%) and Cu (Aldrich 99.99%) foils were used. At etching, the applied voltage was 5 V and the times used were 1, 3, or 6 min. Then the films were annealed at 400°C for 2 h in ambient air.

SEM and EDS studies were done in JSM7800F-JEOL with an additional detector Apollo X 10 mark EDAX. The XRD equipment XPERT MRD, with a pixel detector, three-axis goniometry, a parallel collimator, and a resolution of 0.0001°, was applied to the crystal structure investigation. The Cu source with $K_{\alpha 1}$ line λ = 1.5406 Å was used. XRD was performed for the angle range 20°–80° with a 0.05° step and a step duration of 10 s.

PL spectra, excited by a He-Cd laser with a wavelength of 325 nm and a beam power of 80 mW, were measured at 10–300 K using a PL setup based on a spectrometer SPEX500 described in references [23, 24]. Raman scattering spectra were studied in Jobin-Yvon LabRAM HR 800UV micro-Raman system using an excitation by a solid-state light-emitting diode with a light wavelength of 785 nm [25, 26].

3. The etching time impact on parameters of ZnO NC films

3.1. SEM and XRD studies

Figure 1 presents the SEM images of ZnO NC films grown at different etching times after thermal annealing. It is clear that the size of ZnO NCs decreases versus etching times (**Figure 1d**): from 200–360 nm (for 1 min) down to 30–60 nm (for 10 min).

XRD results are summarized in **Figure 2**. As-grown ZnO films are characterized by the amorphous phase (**Figure 2a**) and the Zn substrate XRD peaks at the 2θ angles of 38.993, 43.233, and 70.058° have been seen (**Figure 2a**). These peaks owe to the diffraction from the (100), (101), and (103) crystal planes in the wurtzite Zn crystal lattice [27].

Thermal annealing at 400°C stimulates the ZnO oxidation and crystallization. A set of XRD peaks appears at the 2θ angles equaling to 31.770, 34.422, 36.253, 47.540, 56.604, and 62.865° after ZnO film annealing (**Figure 2b** and **c**). These XRD peaks correspond to the diffraction from the (100), (002), (101), (102), (110), and (103) crystal planes in the wurtzite ZnO crystal structure [27]. At first (1–6 min etching), the volume of crystalline ZnO phase enlarges that manifests itself in increasing the XRD peak intensities (**Figure 2d**). Then at higher etching time
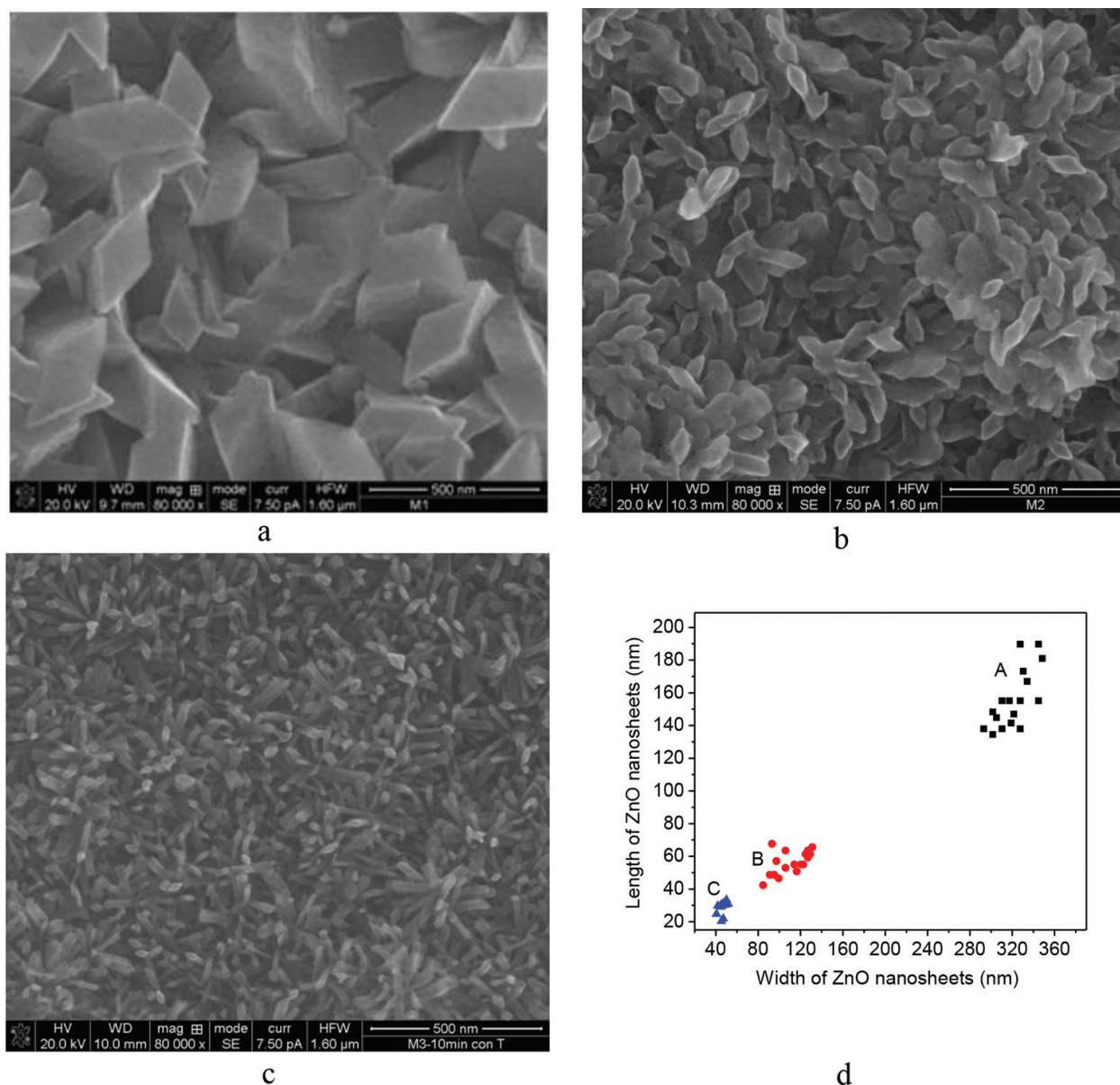
Figure 1. SEM images of ZnO NCs after thermal annealing (a, b, c), obtained at the voltage of 5V and times of 1 min (a), 6 min (b), and 10 min (c). Widths and lengths of annealed ZnO NCs (d) for the etching durations of 1 min (A), 6 min (B), and 10 min (C) [22].

(10 min), ZnO NC films are characterized by smaller XRD peak intensities (**Figure 2d**) owing to, apparently, the material dissolution at the high anodization duration and increasing the volume of pores in the films.

3.2. Raman scattering study

Raman scattering spectra of ZnO NC films are presented in **Figure 3**. Raman spectra of as-grown ZnO films do not demonstrate any Raman peaks (**Figure 3a**). The small Raman band
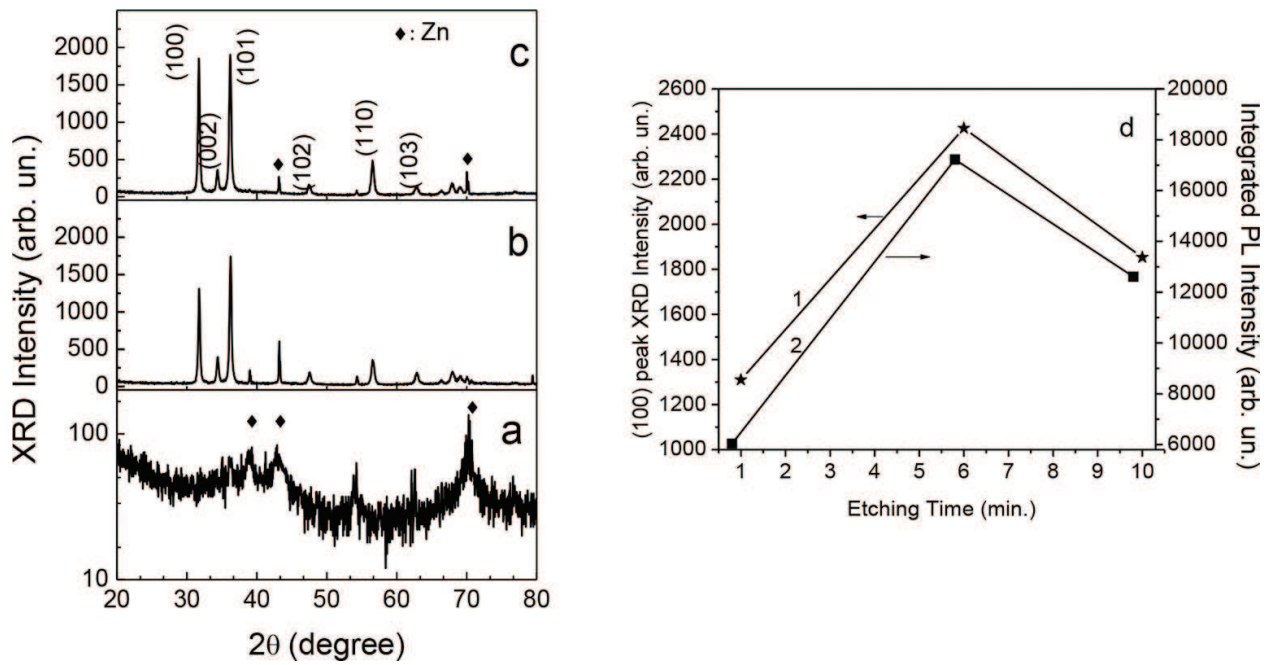
Figure 2. XRD results for as-grown (a) and annealed (b, c) ZnO NCs obtained at etching durations of 1 (b) and 10 (a, c) min. Dependences (d) of (100) XRD peak intensity (1) and integrated PL intensity (2) for the PL band peaked at 3.1 eV in annealed films versus etching times [22].
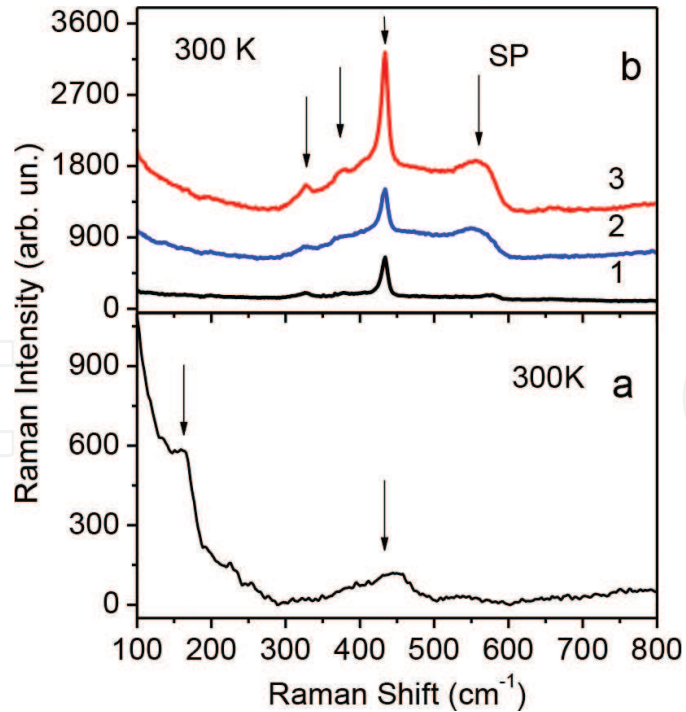

Figure 3. Raman scattering spectra of as-grown (a) and annealed (b) ZnO films obtained at etching times: 1 min (curve 1), 6 min (curve 2), and 10 min (a) and (b), curve 3.

in the range of 400–500 cm^{-1} is related to Raman scattering in the ZnO amorphous phase. The Raman study confirms that as-grown ZnO films are characterized by an amorphous phase mainly and it is consistent with the XRD data.

Annealing at 400°C stimulates the ZnO crystallization and four peaks at 327, 379, 434, and 549–556 cm^{-1} appear in Raman spectra (**Table 1**). The Raman peak intensity rises versus etching time owing to the volume enlargement of the crystalline ZnO phase (**Figure 3b**).

The group theory predicts for the wurzite ZnO crystal structure the Raman active phonons in Brillouin zone center as: A_1 and E_1 symmetry polar phonons with two frequencies for the transverse (TO) and longitudinal (LO) optic phonons, and E_2 symmetry nonpolar phonon mode with two frequencies E_2 (low) and E_2 (high). E_2 (low) and E_2 (high) modes are attributed to oxygen and zinc sublattices, respectively, in ZnO [28, 29].

Raman peaks at 327 and 437 cm^{-1} are attributed, as a rule, to second-order Raman peaks arising from the zone boundary phonons $3E_{2H}$-E_{2L} and E_{2H} modes in ZnO NCs [30]. Raman peaks at 379 and 434 cm^{-1} can be attributed to the A_1 (TO) and E_2 (high) phonon modes in ZnO NCs (**Table 1**). The nature of the Raman peak at 549–556 cm^{-1} is not clear. Its variable position in different samples (**Figure 3**, curves 2 and 3) and the location between TO and LO optic phonons permit to assign this Raman peak to the surface phonon (SP). The SP frequency (ω_{SP}) in ZnO NCs can be calculated using the formula [30, 31]:

$$\omega_{SP} = \omega_{TO} \sqrt{\frac{\varepsilon_0 l + \varepsilon_M(l+1)}{\varepsilon_\infty l + \varepsilon_M(l+1)}}, \tag{1}$$

where ω_{TO} is a frequincy of TO phonon, ε_0 and ε_∞ are the static and high-frequency dielectric constants in a bulk ZnO crystal, ε_M is a static dielectric constant of surrounding medium (air). Assuming $\varepsilon_M = 1$ for air in pores of ZnO NCs and using ε_0 and ε_∞ equal to 8.36 [32] and 3.77 [32], respectively, the SP frequency of 550 cm^{-1} for the lowest (l = 1) mode has been estimated that is in a good agreement with detected values of 549–556 cm^{-1} (**Table 1**).

3.3. ZnO NC emission study

PL spectra of ZnO films obtained at different etching times in as-grown states are shown in **Figure 4**. PL spectra are presented as the superposition of three PL bands centered at 1.90–2.03, 2.49–2.51, and 2.80–2.85 eV (**Figure 4**, curves a, b, and c), which are attributed to the defect-related emission in an amorphous ZnO films. The PL intensity of the above-mentioned peaks increases with increasing anodization duration up to 6 min due to increasing the volume of ZnO amorphous phase. In samples prepared at 10 min (**Figure 4**, curve 3), the PL

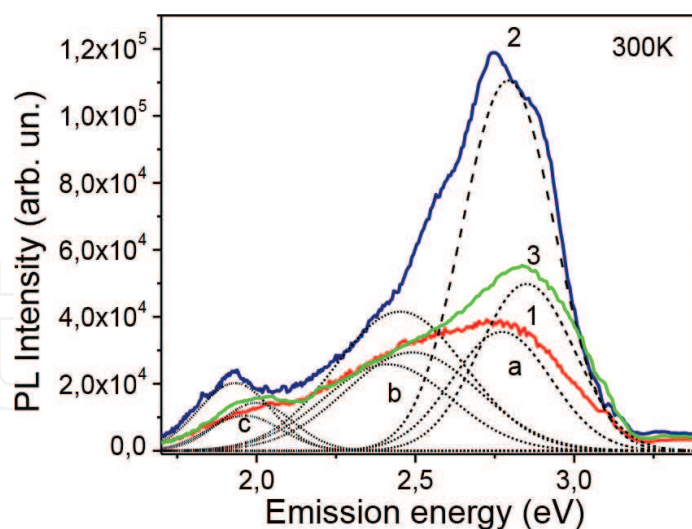| Samples	E_2(low)	$3E_{2H}$-E_{2L}	A_1(TO)	E_1(TO)	E_2(high)	SP	A_1(LO)	E_1(LO)
	cm^{-1}	cm^{-1}	cm^{-1}	cm^{-1}	cm^{-1}	cm^{-1}	cm^{-1}	cm^{-1}
Bulk ZnO [29] and ZnO NCs	102	327	379	410	434–439	549–556	574	591

Table 1. Raman peaks in ZnO crystals.

Figure 4. PL spectra of as-grown ZnO NCs obtained at durations of 1 (1), 6 (2), and 10 (3) min. Dashed curves represent the deconvolution result on elementary PL bands (a, b, c).

intensity of the mentioned PL peaks decreases owing to decreasing the ZnO NC volume that is consistent with the XRD data (**Figure 2**).

Annealing at 400°C stimulates the ZnO crystallization, which is accompanied by the PL spectrum transformation (**Figure 5**). PL spectra of ZnO NCs are complex as well (**Figure 5**, curves 1, 2, and 3) and can be represented by a set of elementary PL bands (**Figure 5**, curves a, b, and c) with the peaks at 2.06–2.10, 2.52, and 3.10 eV. The defect-related PL band with the peak at 2.80 eV disappeared completely at the ZnO oxidation and crystallization, and the new PL band at 3.10 eV appeared in PL spectra of ZnO NCs. PL intensities of the mentioned PL bands (**Figure 5**) vary as XRD peak intensity changes, which is related to the changing crystalline ZnO volume versus anodization times (**Figure 2**d).
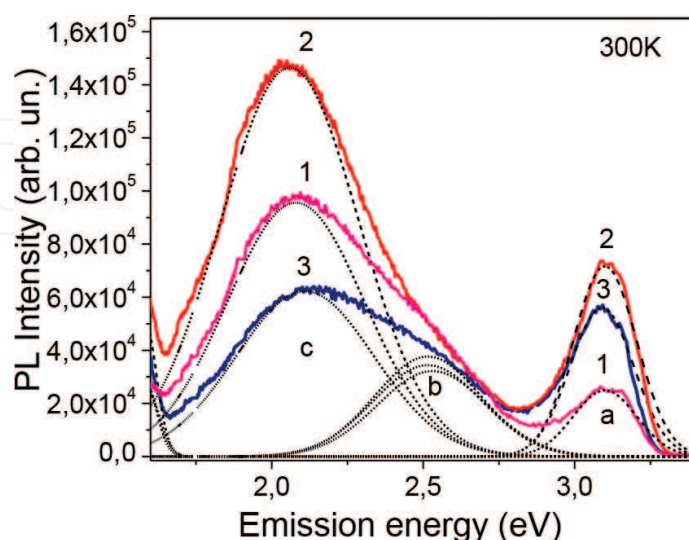

Figure 5. PL spectra of annealed ZnO NCs obtained at durations of 1 (1), 6 (2), and 10 (3) min. Dashed curves represent the deconvolution on elementary PL bands (a, b, c) [22].

The bulk ZnO crystals are characterized by the variety of luminescence bands in UV and visible spectral ranges [33, 34]. The origin of these emissions has not been conclusively established, and a number of hypotheses have been proposed for each emission band. NBE band at 3.1 eV is attributed to the optical transition between the shallow donor and valence band, to the phonon replicas of bound exciton, or free exciton (FE) emissions [34, 35]. The high intensity of NBE emission at 300 K and a small band half width in ZnO NCs permits to attribute the 3.1 eV PL band to a LO phonon replica of free exciton.

The blue PL band with the peak at 2.80 eV, which disappeared completely after the oxidation at annealing in ambient air, can be assigned to emission via the native defects in ZnO films [36, 37]. The defect-related green PL band in the range 2.40–2.50 eV is assigned to oxygen vacancies [36], Cu impurities [38], or surface defects [39] in ZnO. The PL intensity of 2.49–2.52 eV PL band does not change in the processes of oxidation and crystallization (**Figure 5**) that permits to assign this PL to some surface defects.

The PL band centered at 2.00–2.10 eV was assigned earlier to interstitial oxygen atoms (2.02 eV) [40] or hydroxyl groups (2.10 eV) [41, 42]. The PL intensity of 2.06–2.10 eV PL band increases at ZnO oxidation (**Figure 5**) and the assumption that corresponding defects are related to oxygen interstitials looks very reliable.

It is essential that ZnO NCs obtained by other methods, such as Zn powder thermal evaporation [43], sol-gel ZnO films [44], or MOCVD growth ZnO films [45], do not permit to obtain great variety of PL bands that have been demonstrated in the studied ZnO NCs.

4. Anodization voltage impact on the structure and emission of ZnO NC films

4.1. XRD and SEM study

The XRD study has shown that as-grown ZnO films are characterized by Zn substrate-related XRD peaks with highest XRD peak intensities at the angles 2θ equal to 38.993, 43.233, and 70.058° (**Figure 6a**). These peaks correspond to the diffraction from the (100), (101), and (103) crystal planes, respectively, in the hexagonal Zn crystal lattice with the lattice parameters of a = 2.6650 Å and c = 4.9470 Å [27]. Annealing at 400°C stimulates the crystallization of ZnO NCs and a set of XRD peaks appear at the angles 2θ equal to 31.770, 34.422, 36.253, 47.540, 56.604, and 62.865° (**Figure 6b**). These XRD peaks correspond to the X-ray diffraction from the (100), (002), (101), (102), (110), and (103) crystal planes in the wurtzite ZnO crystal structure [27].

The volume of crystalline ZnO phase enlarges versus anodization voltages up to 15 V that manifests itself by increasing the XRD peak intensities. However, ZnO NCs obtained at the voltage of 20 V are characterized by smaller intensity of XRD peaks that, apparently, connects with the ZnO dissolution in an electrolyte at higher anodization voltages and increases the volume of the pores.

SEM images after thermal annealing of ZnO NCs, obtained at voltages of 1, 5, and 15 V, are presented in **Figure 7(a)–(c)**. The dimension of ZnO NCs does not change essentially versus
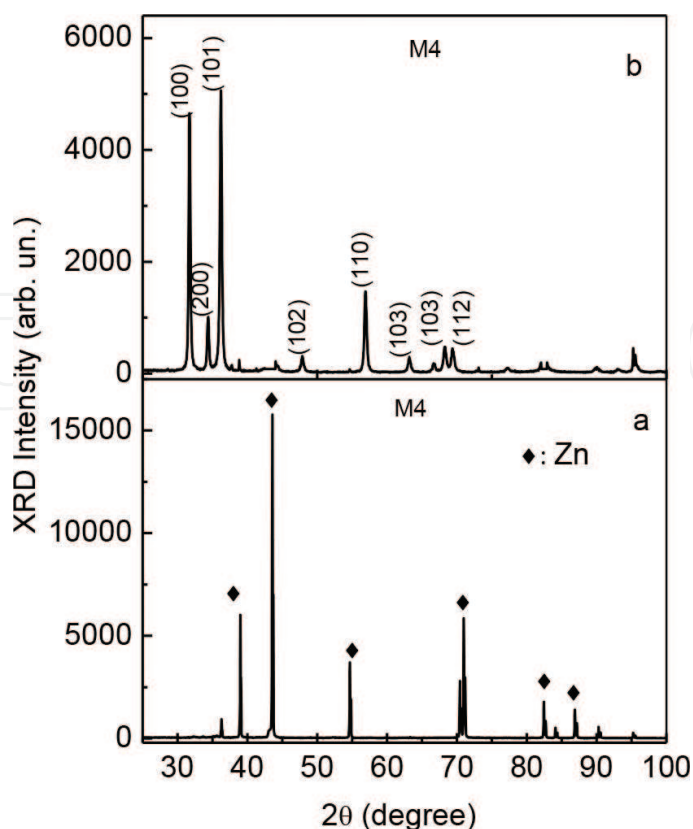
Figure 6. XRD results for as-grown film (a) and annealed (b) ZnO NCs prepared at etching voltage 15 V and etching time 6 min [24].

voltages at the anodization (**Figure 7d**). The sizes estimated from SEM images vary in the range 45–60 nm up to 85–105 nm. Anodization voltage increase leads to a raise in the thickness of ZnO NC layers mainly.

4.2. Emission study of ZnO NCs

PL spectra of ZnO NCs prep ared at different anodization voltages and annealed at 400°C are complex and can be presented as a set of PL bands. The deconvolution procedure permits to obtain the PL bands centered at: 3.18, 3.02, 2.94, 2.55, and 1.98 eV (**Figure 8**).

Elementary PL bands with the peaks at 2.55 and 1.98 eV were attributed earlier to the defect-related emissions in ZnO NCs [33–36]. The intensity of defect-related PL bands enlarges with increase in the anodization voltages due to increase in the volume of ZnO NC layers. The high energy PL bands (3.18, 3.02, and 2.94 eV) were assigned to NBE emission in ZnO [31].

PL spectra of ZnO NCs measured in the temperature range 10–300 K are presented in **Figure 9**. The intensities of defect-related PL bands (1.98 and 2.55 eV) decrease significantly in this temperature range. Integrated PL intensities versus temperature have been presented in Arrhenius coordinates in **Figures 10** and **11** with the aim to estimate the activation energies of PL thermal decays.
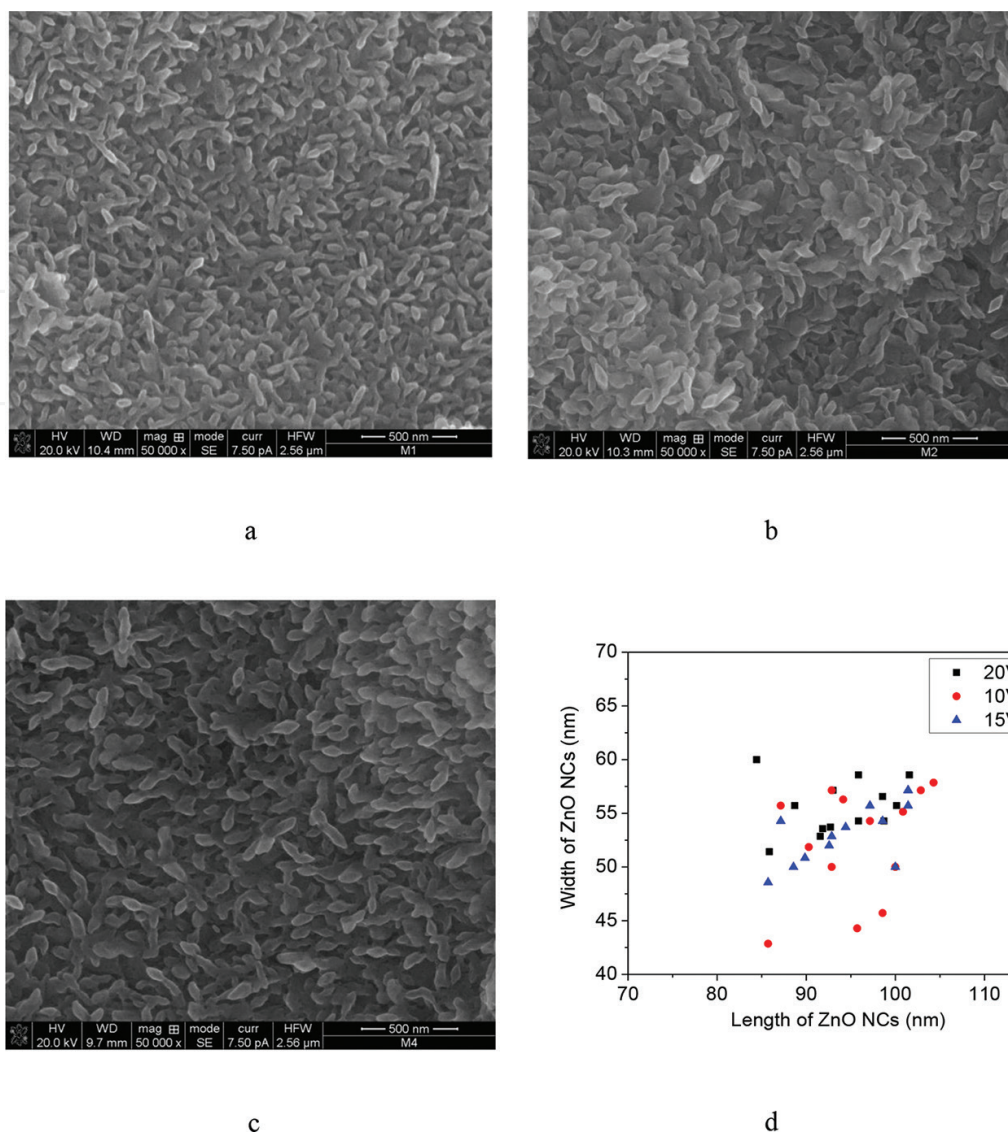
Figure 7. SEM images of annealed ZnO NCs obtained at anodization voltages 1 (a), 5 (b), and 15 V(c) for etching time 6 min. Widths and lengths of annealed ZnO NCs (d) obtained at different etching voltages of 10, 15, and 20 V [24].
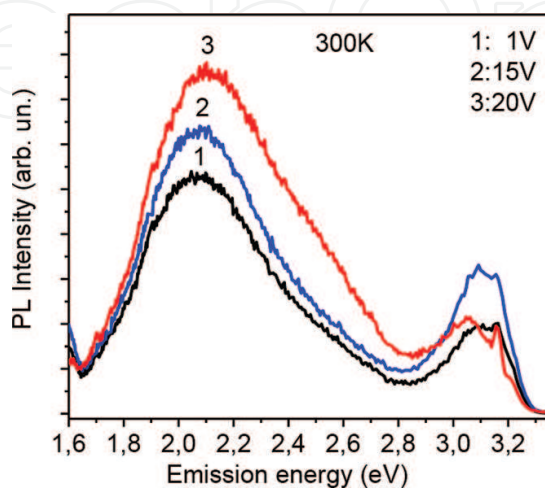

Figure 8. PL spectra of ZnO NCs prepared at voltages: 1 (1), 15 (2), and 20 (3) V.
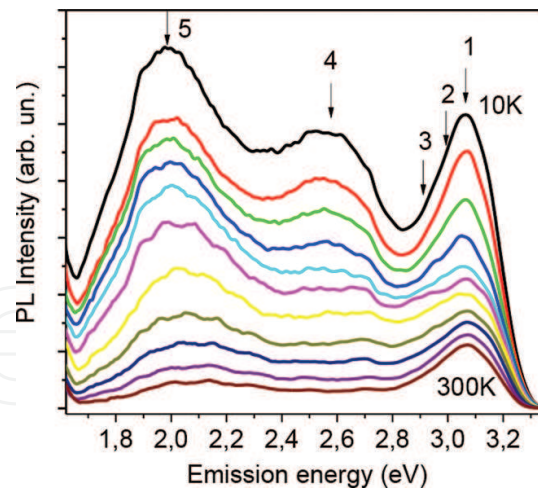
Figure 9. PL spectra of ZnO NCs obtained at 15 V and measured at 10–300 K with the step of 30 K.
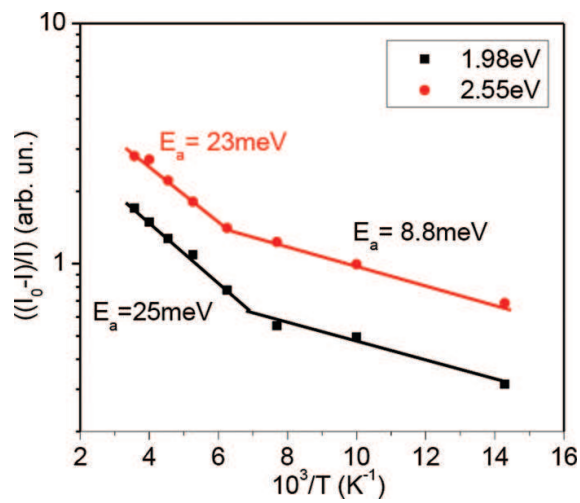

Figure 10. Dependences of integrated PL intensities versus temperature presented in Arrhenius coordinates for defect-related PL bands.
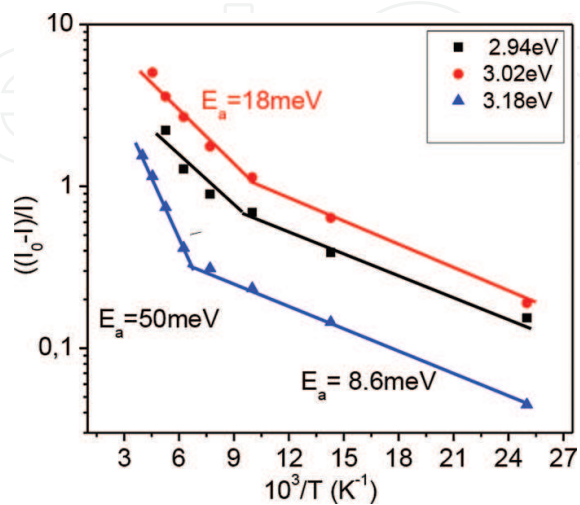

Figure 11. Dependences of integrated PL intensities versus temperature presented in Arrhenius coordinates for NBE emission bands.

PL thermal decays in the range 10–150 K for all PL bands realize with the same activation energy (8.6–8.8 meV) due to the activation, apparently, of some nonradiative recombination centers. Thermal quenching of all PL bands starts at higher temperatures (150–300 K). The 2.94 and 3.06 eV PL bands, which demonstrate the PL thermal decay with the activation energy of 18meV, are related, apparently, to the LO phonon replicas of bond-exciton emission. The 3.18 eV PL band, with highest PL decay activation energy (50 meV), is connected, probably, with the LO phonon replicas of FE emission.

5. Size-dependent effects in emission of ZnO NC films

The impact of NC sizes on PL spectra has been studied using ZnO NCs prepared at a voltage of 5 V, times: 1 (1), 3 (2), 6 (3), and 10 (4) min and annealed at 400°C. These ZnO NCs have been discussed in Section 3 and their sizes are summarized in **Table 2**. PL spectra of these ZnO NCs are a superposition of PL bands with the peaks at 2.05, 2.45, and 3.11 eV (**Figure 12**, dashed lines).

Figure 13 shows the variation of NBE emission in ZnO NCs of different sizes. The 3.10 eV PL band at 300 K belongs to the FE phonon-assisted replica in ZnO NCs [21, 22]. The deconvolution procedure has been applied to PL spectra and its result is presented by dashed curves in **Figure 13**. PL bands centered at 3.010, 3.082, 3.154, and 3.226 eV were chosen for the deconvolution, which can be attributed to the LO phonon replicas (FE-5LO, −4LO, −3LO, and −2LO) of A exciton (3.373 eV). The energy difference between these PL transitions is close to some numbers of LO phonons (72 meV) in ZnO [46].

Integrated PL intensities of 2.45, 3.010, 3.082, 3.154, and 3.226 eV PL bands increase significantly with diminishing the ZnO NC size and with enlarging the surface-to-volume ratio (**Figure 14a** and **b**).

Additionally, the main PL peak of NBE emission shifts to higher energy owing to the PL intensity enlargement of 3LO and 2LO phonon replicas mainly (**Figure 13**). Note that PL spectra of ZnO NCs, typically, do not reveal any FE peaks or phonon replicas owing to poor material quality and high concentrations of structural defects.

Sample numbers	Average NC width (nm)	Average NC length (nm)	Lattice parameter, "a" (Å)	Lattice parameter, "c" (Å)	Porosity, c_0 (%)
Bulk ZnO [27]			3.2495	5.2069	
1	308	600	3.2504	5.2071	25
2	253	459	3.2534	5.2119	28
3	170	316	3.2564	5.2167	37
4	67	131	3.2584	5.2199	50

Table 2. The size of ZnO NCs from SEM images and hexagonal crystal lattice parameters estimated from XRD data.
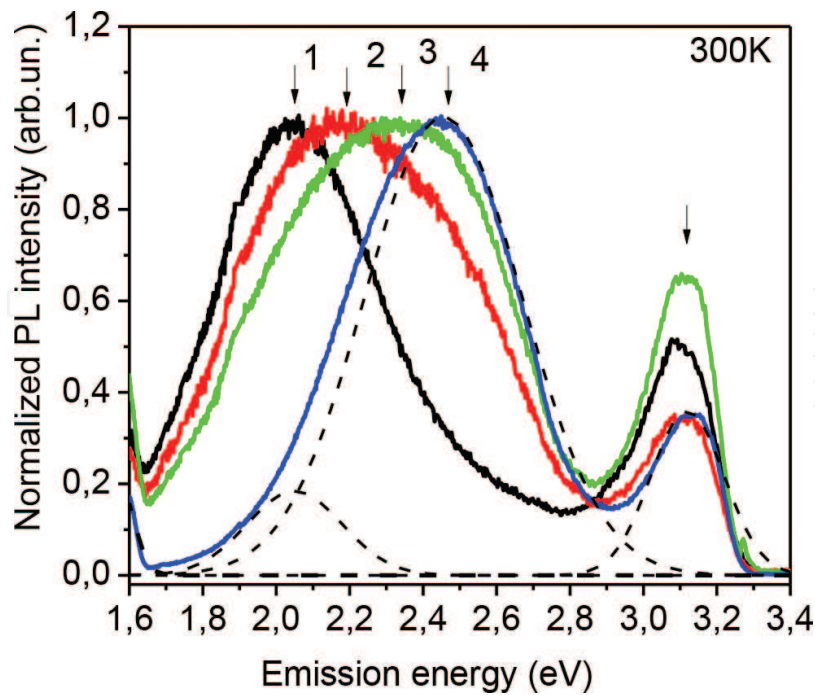
Figure 12. Normalized PL spectra of ZnO NCs obtained at times of 1 (1), 3 (2), 6 (3), and 10 (4) min. Dashed curves present the deconvolution of the PL spectrum (4) [26].

The defect-related green PL band, detected traditionally in the spectral range of 2.40–2.50 eV in ZnO, has been assigned to the oxygen vacancies [36], Cu impurities [38], or surface defects [22, 39]. In our experiments, the intensity of 2.45 eV PL band increases significantly (**Figure 14a**) in PL spectra at decreasing the ZnO NC size and increasing the surface-to-volume ratio in NCs. Thus, it can be supposed that emission centers, responsible for the 2.45 eV PL band, relate to the surface defects and their concentration enlarges with increasing the surface-to-volume ration in ZnO NCs.

5.1. NBE intensity stimulation at ZnO NC size decreasing

The intensity of 3.082–3.226 eV PL bands, related to FE phonon-assisted replicas, increases significantly with decreasing the ZnO NC size (**Figure 14b**). Since the process of reduction in size is accompanied by increasing the interplanar distances in ZnO NCs (**Table 2**), the FE-related PL bands have to shift to lower energy in small NCs (4). But the main PL peak of NBE emission shifts to high energy (**Figure 13**) from 3.08 eV (1) to 3.14 eV (4). It means that some other physical mechanism is responsible for the PL intensity enlargement and spectral transformation of NBE emission band.

The PL intensity W_{PL} of ZnO NCs can be represented by the formula [47]:

$$W_{PL} = I_0(1-R)^2(1-c_0)[1-\exp(-\alpha d)]\eta \tag{2}$$

where I_0 is the excitation light intensity, d is the ZnO NC layer thickness, R and α are the reflection and absorption coefficients, and η is the internal quantum emission efficiency that is ($\eta = \frac{\tau_R^{-1}}{\tau_R^{-1}+\tau_{NR}^{-1}}$), τ_R and τ_{NR} are radiative and nonradiative recombination times, respectively,
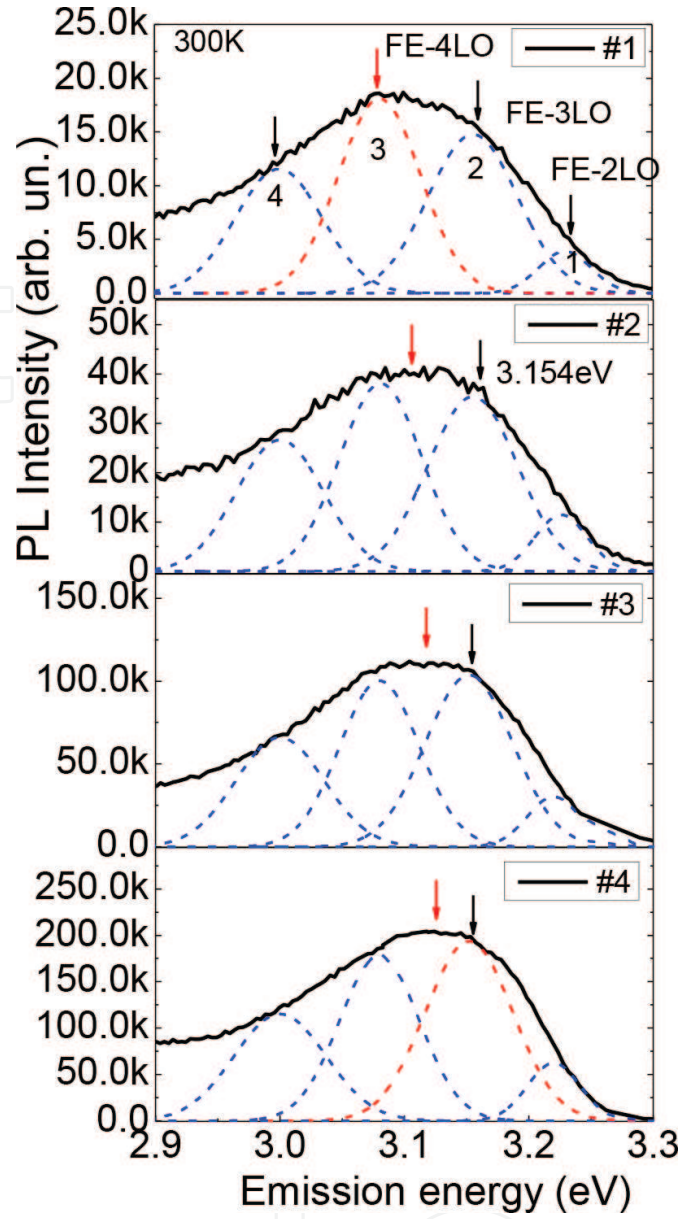
Figure 13. NBE emission bands in annealed ZnO NCs obtained at the durations of 1 (1), 3 (2), 6 (3), and 10 min (4). Dashed curves present the deconvolution of PL spectra on LO phonon-assisted PL bands [26].

and c_0 is the porosity of ZnO layers (**Table 2**). At high porosity, the ZnO volume, which absorbs the excitation light, decreases.

Let us consider the coefficients of relative varying the integrated PL intensities in the studied structures, in comparison with the structure 1, at permanent parameters of the excitation light intensity (I_0) and R coefficient. Actually, the excitation intensity I_0 was the same in our experiments and the reflection coefficient decreases a little versus NC sizes in the range 60–600 nm. The relation of PL intensities can be presented as:

$$K_{ex} = \frac{W_{PL}^{\#i}}{W_{PL}^{\#1}} = \frac{(1 - c_{oi})}{(1 - c_{o1})} \frac{[1 - \exp(-\alpha\, d_i)]\eta_i}{[1 - \exp(-\alpha\, d_1)]\eta_1} \tag{3}$$
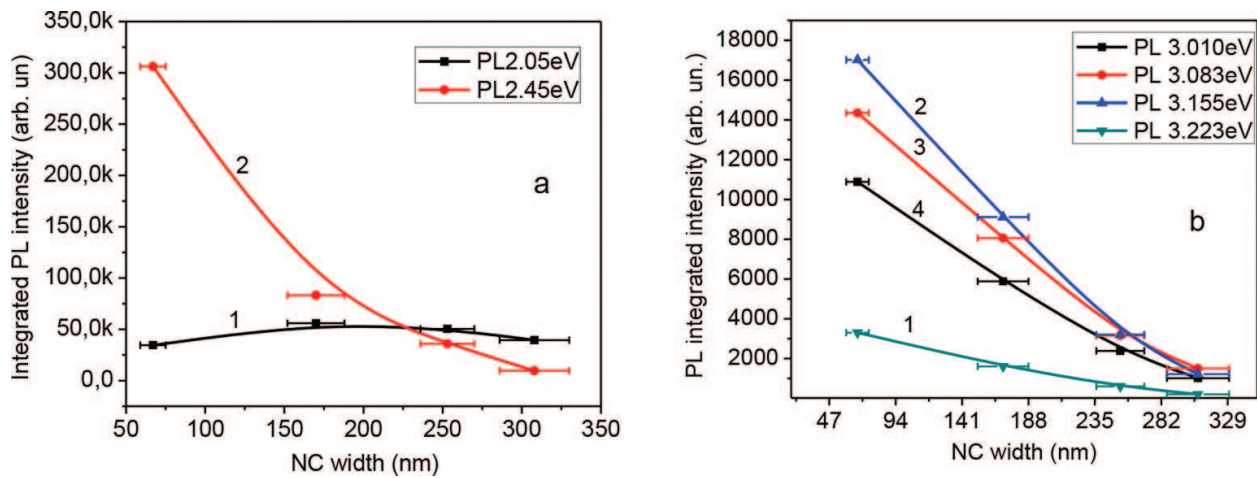
Figure 14. The variation of integrated PL intensities versus sizes of ZnO NCs for PL bands: (a) 2.05 (1) and 2.45 (2) eV and (b) 3.226 (1), 3.154 (2), 3.082 (3), and 3.010 (4) eV [26].

The values of K_{ex} parameters are summarized in **Table 3**. Some rising in exciton PL intensity in ZnO NCs at the NC size variation from 308 × 600 nm (1) down to 253 × 459 nm (2) can be explained by increasing the NC layer thickness and excitation light absorption. However, the PL intensities of all PL bands enlarge significantly (**Figure 14**, **Table 3**) when the size of ZnO NCs decreases down to 67 × 131 nm (4). To explain the reasons of such PL stimulation, the factors that influent on the internal quantum efficiency and radiative recombination rates have to be discussed.

The stimulation of internal quantum efficiency in small ZnO NCs (3, 4) can be attributed to exciton recombination rate increasing owing to the realization of the weak exciton confinement. The theoretical consideration of this effect was presented in references [48, 49] and two regimes of weak exciton confinement are discussed. The first regime deals with NCs of the size "bigger" than the Bohr exciton radius, but "smaller" than a wavelength of emitted light in ZnO. Oscillator strength increase in the first case is a result of oscillator strength enhancement for localized excitons in proportion to spreading their wave functions, predicted for the bound exciton early [50].

N	PL K_{ex} 3.226 eV	PL K_{ex} 3.155 eV	PL K_{ex} 3.083 eV	PL K_{ex} 3.010 eV	PL K_{ex} 2.45 eV	Average NC width, nm
1	1.0	1.0	1.0	1.0	1.0	308
2	2.9	2.6	2.1	2.3	3.7	253
3	7.8	7.5	5.4	5.8	8.6	170
4	16.0	14.0	9.5	10.7	31.6	67

Table 3. Experimental rations K_{ex} for integrated PL intensities W_i/W_1 of studied PL bands.

The second weak confinement regime is connected with exciton-light coupling with the formation of polaritons, which becomes strong if the size of NCs approaches to light wavelength in ZnO. The exciton recombination rate G, at the assumption of exiton-light coupling was considered as the product of photon and exciton eigenstates early in [48, 49]:

$$G = K \left[\int dr \cos(kr) \, \Phi(r) \right]^2, \text{ with } k = \sqrt{\varepsilon_\infty} \, k_o \tag{4}$$

where k is the wave vector of light in a material with the high frequency dielectric constant, ε_∞, that equals to $\varepsilon_\infty = 3.77$ [32] in ZnO, $k_0 = 2\pi/\lambda_0$ is the wave vector of light at an exciton resonance frequency and K is a characteristic of long-range exchange energy splitting for exciton in NCs [48]. The $\Phi(r)$ in Eq. (4) was taken as a Gaussian function to get an analytical formula and formulas for the exciton recombination rate G and exciton recombination time τ_R were obtained as [48, 49]:

$$G = \frac{\sqrt{2\pi}}{12} \, \omega_{LT} \left(\frac{2\pi}{\lambda_o} \right)^3 \langle r \rangle^3 \exp\left(-8 \, \varepsilon_\infty \frac{\pi^2 \langle r \rangle^2}{\lambda_o^2} \right) \tag{5}$$

$$\tau_R = \frac{1}{G} \tag{6}$$

The radiative recombination rates (**Figure 15**) and corresponding radiative lifetimes (**Figure 16**) have been numerically estimated using Eqs. (5) and (6) for the quant energy of FE phonon-assisted replicas (3.226, 3.154, 3.082, and 3.010 eV) in ZnO NCs of different sizes.

The recombination rates approach to maximum in ZnO NCs with diameters of 59–64 nm for the exciton-light coupling model (**Figure 15**) and starting from 59 to 64 nm the radiative recombination rate decreases (radiative lifetime increases) versus NC sizes (**Figures 15** and **16**).

The estimation of exciton recombination rates (**Figure 15**) has been done for the spherical shape of NCs. In the studied films, the ZnO NCs have a rhomb shape (**Figure 1**). The exciton
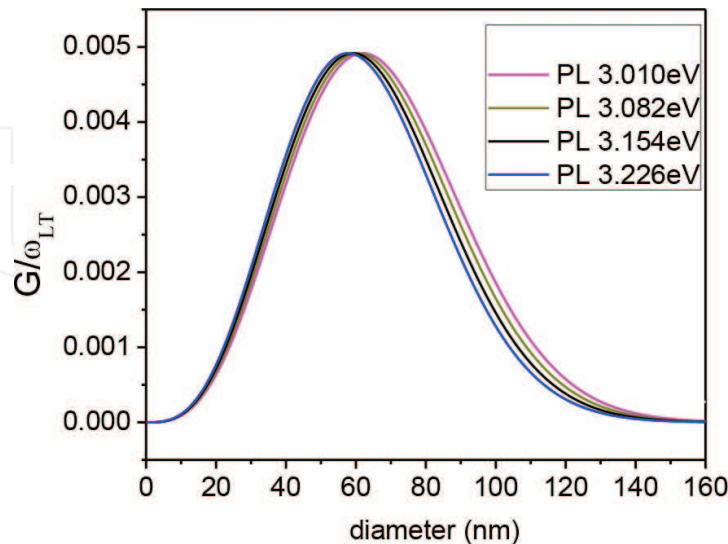

Figure 15. Numerically simulated exciton recombination rates for LO phonon-assisted PL bands in ZnO NCs of different sizes [26].
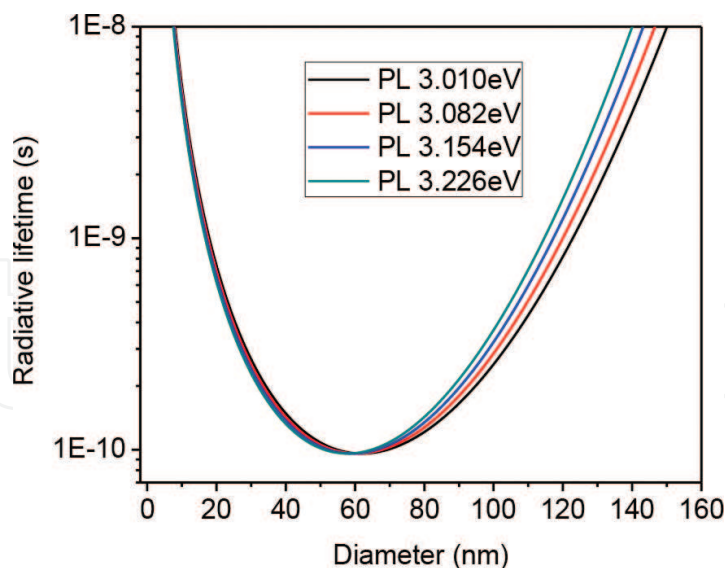
Figure 16. Numerically simulated exciton radiative lifetimes for LO phonon-assisted PL bands in ZnO NCs of different sizes [26].

recombination rate decreases fast versus sizes (**Figure 15**) and due to this is reasonable to consider only the smallest NC parameter (width), because the recombination rate along the largest NC sizes (length) will be some orders smaller. Thus, the variation of PL intensity in ZnO NCs is reasonable to present versus NC widths, as shown in **Figure 14**.

The exciton-light coupling model predicts well the ZnO NC size (59–64 nm), where the maximum of PL intensity can be expected. This size correlates with the NC width (67 nm) in the structure 4 with highest detected PL intensity. However, the PL intensities of FE phonon-assisted PL bands enlarge 15- or 10-fold with decreasing NC widths from 250 down to 67 nm (**Table 3**). At the same time, the estimated recombination rate has to increase 90-fold or even more in the proposed model (**Figure 15**). This difference can be attributed to the following reasons: (i) the enlargement of nonradiative recombination rate in smallest ZnO NCs due to increasing significantly the concentration of surface defects and (ii) the exciton-light coupling and polariton orientation partially along the length of ZnO NCs, where the exciton recombination rate is smaller. Thus, the stimulation of both recombination parameters τ_{R}^{-1} and τ_{NR}^{-1} with decreasing ZnO NC sizes and random polariton orientation in ZnO NCs lead to smaller internal quantum efficiency, η, and integrated PL intensity, W_{PL}, than it is predicted by the exciton-light coupling model.

We need to discuss as well increasing the integrated PL intensity of FE-2LO and FE-3LO replicas in comparison with the intensity of FE-4LO and FE-5LO bands (**Figure 13**, **Table 3**) in small ZnO NCs. This effect, probably, deals with decreasing the exciton-phonon coupling strength in the smallest ZnO NCs that were predicted early for ZnO QDs [51]. The effect was attributed to diminishing exciton polarity in small NCs and to decreasing Frohlich polar intraband scattering that induces phonon-assisted emission bands [52–54].

6. Impact of Cu-doping on the structure and emission properties of ZnO NC films

To the adjustment of ZnO NC characteristics the doping by different metals Al [55], Co [56], Ni [57], Cu [58, 59], or Ag [60] can be used. Cu atoms are most impotent impurities due to the low toxicity and large source content. ZnO:Cu NCs have demonstrated excellent electrical, magnetic, and photoelectrical characteristics and gas sensing [58, 59]. The Cu atoms are well known as emission activators for semiconductors that can change essentially the emission intensity in ZnO NCs [58, 59].

A lot of papers related to doping ZnO films by Cu in different concentrations were published recently [61–64]. A systematic change of XRD parameters with Cu content increasing in the ZnO crystal lattice was observed in Ref. [63], together with decreasing the ZnO energy band gap versus Cu contents [63]. NBE intensity enhancement in ZnO films with Cu doping at 2.0 at% and emission quenching at Cu doping 4.4 at% was reported in Ref. [56].

A set of published papers are devoted to the defect study if the ZnO:Cu crystals [64, 65]. The green PL band at 2.45 eV with the LO phonon-related structure and zero-phonon line was assigned to the optical transition via Cu_{Zn} acceptors [64, 65]. The structure-less green emission was assigned to the recombination of electron from a shallow donor with hole bounds to Cu+ ions [65].

The assumptions concerning the Cu defect structure have been presented, but only some of them look as reliable. The purpose of our work is connected with the investigation of correlated varying the XRD parameters and PL spectra of ZnO Cu NCs versus Cu contents with the aim to analyze the Cu-related defects. The parameters of the studied ZnO and ZnO Cu NCs are summarized in **Table 4**.

6.1. SEM and XRD studies

SEM images of ZnO and ZnO Cu NCs obtained at the adonization duration of 3 min with thermal treatment at 400°C are presented in **Figure 17(a)** and **(b)**. ZnO NCs have a rhomb

Sample number	Type of NCs	Etching duration (min)	Etching voltage (V)	NC size (nm)	Integrated PL intensity of all bands at 10 K (arb. un.)
1	ZnO	1	5	308 × 548	1.0×10^5
2	ZnO	3	5	273 × 459	2.0×10^5
3	ZnO	6	5	170 × 316	2.4×10^5
4	ZnO Cu	1	5	300 × 540	1.3×10^5
5	ZnO Cu	3	5	282 × 510	3.3×10^5
6	ZnO Cu	6	5	200 × 320	1.7×10^5

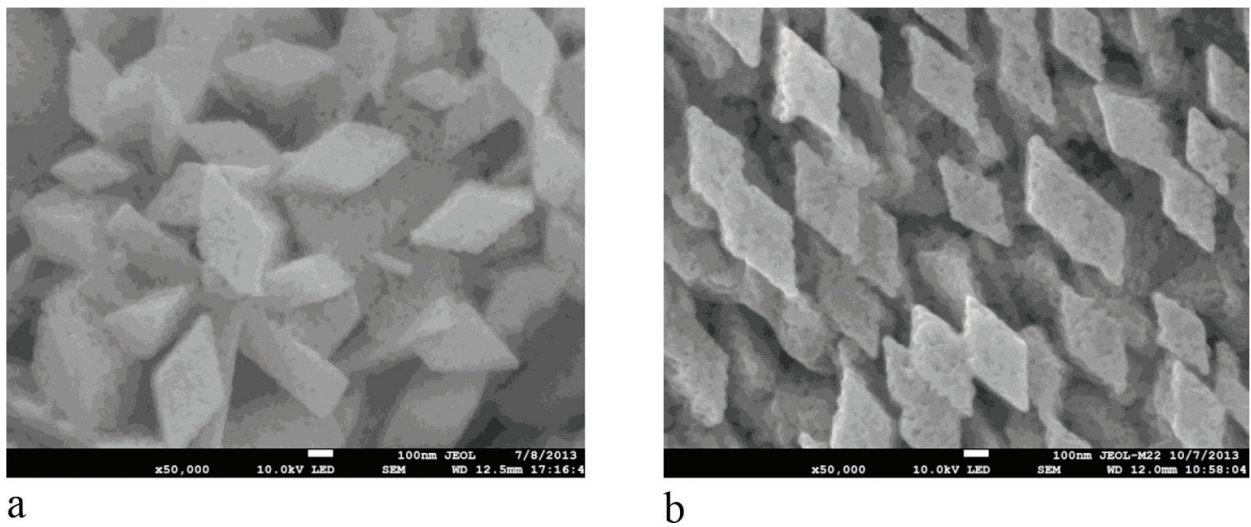**Table 4.** The average NC sizes obtained from SEM images.

Figure 17. SEM images of N2 ZnO NCs (a) and N5 ZnO Cu (b) NCs obtained at an anodization time of 3 min after thermal annealing.

shape and we used width and length for the size characterization (**Table 4**). The size of ZnO NCs decreases versus etching times from 308 × 548 nm to 170 × 316 nm (**Table 4**).

At first, the XRD investigation of ZnO and ZnO Cu NCs has been done with the aim to confirm that Cu atoms are incorporated in ZnO NCs. The five XRD peaks have been detected in both types of NCs (**Figures 18** and **19**), related to the diffraction from the (100), (002), (101), (110), and (103) crystal planes in the wurtzite ZnO crystal lattice [27].
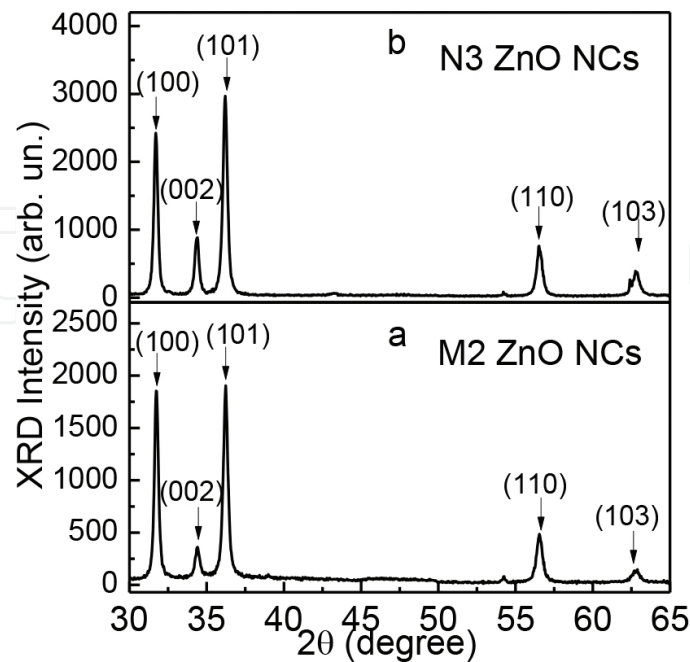

Figure 18. XRD results for the N2 (a) and N3 (b) ZnO NCs (Table 4) after thermal annealing [66].
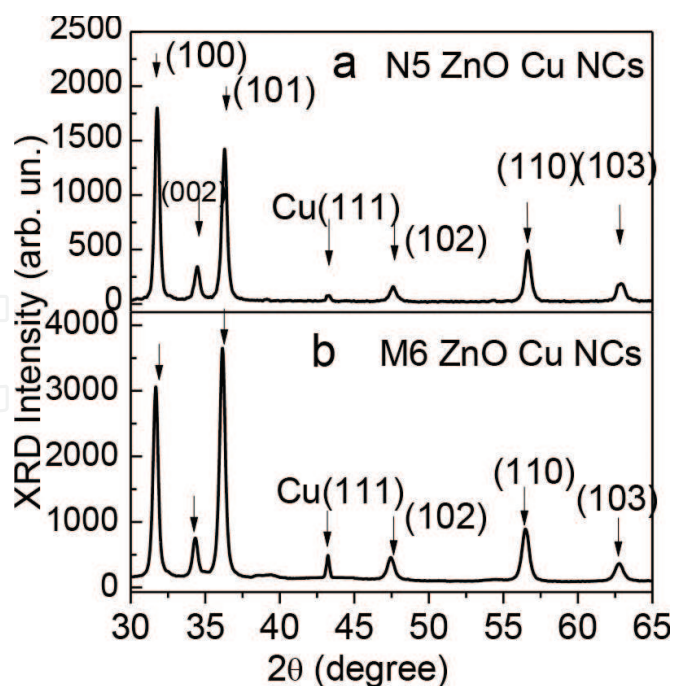
Figure 19. XRD results for the N5 (a) and N6 (b) ZnO Cu NCs (Table 4) after thermal annealing [66].

The decreasing ZnO NC size stimulates the shift of XRD peaks to lower angles (**Table 5**) that testify on larger interplane distances in small ZnO NCs. It was supposed early that this effect is related to compressive strain decreasing in small ZnO NCs [26].

At the XRD study of ZnO:Cu NCs with small Cu concentration of ≤2.28 at% [67] (samples N4 and N5), the XRD peaks shift to bigger diffraction angles (2 theta) in comparison with ZnO NCs (samples N1, N2), together with decreasing the NC sizes (**Table 5**). This effect testifies on smaller interplanar distances in ZnO:Cu NCs. At the Cu concentration higher than 2.28 at% (sample N6), XRD peaks shift to smaller 2 theta values even more essential than those are detected in ZnO NCs (sample N3). The last effect corresponds to increasing the interplanar space in ZnO Cu NCs of N6.

Sample number	ZnO (100)	ZnO (002)	ZnO (101)	Cu (111)	ZnO (110)	ZnO (103)
1	31.7622	34.4022	36.2322		56.5422	62.8922
2	31.7322	34.4022	36.2321		56.5422	62.8922
3	31.7022	34.3722	36.2022		56.5222	62.8822
4	31.7713	34.4663	36.2793		56.6143	62.8473
5	31.7813	34.4763	36.2893	43.2963	56.6733	62.8963
6	31.6891	34.3351	36.1481	43.2531	56.4831	62.8041

Table 5. XRD peaks for studied ZnO NCs and ZnO Cu NCs [66].

The valence of Cu could be +1 or +2 and the radius of Cu^+, Cu^{+2}, and Zn^{+2} ions are 0.096, 0.072, and 0.074 nm, respectively, in ZnO [68–72]. Substitution ions Cu^+ and Cu^{+2} and interstitial Cu^{+2} ions can be incorporated in ZnO. Lattice constants in ZnO:Cu NCs increase, in comparison with those in undoped ZnO NCs, when Cu^+ substituted Zn^{+2} ions, together with compressive strain enlarging [68, 69]. In ZnO:Cu nanowires (NWs), a decrease in lattice parameter was detected and interpreted as Cu^{+2} ions substituted of Zn^{+2} ions in ZnO [70]. In addition, Cu atoms can form the complex defects $[Cu_{Zn} Zn_i]_x$ as well [70].

In our study of ZnO and ZnO:Cu NCs three XRD effects have been revealed:

1. A low angle shift of XRD peaks in ZnO NCs at decreasing NC sizes (**Table 5**) owing to compressive strain decreasing that can be accompanied by decreasing the energy band gap.

2. A higher angle shift of XRD peaks at small Cu content (2.28 at%) in ZnO:Cu NCs (**Table 5**) owing to, probably, the Cu^{+2} ion substitution of Zn^{+2} ions in ZnO.

3. A low angle shift of XRD peaks at higher Cu content (≥2.28 at%) in ZnO Cu NCs (**Table 5**) owing to Cu^+ ion substituting the Zn^{+2} ion or the formation of Cu-related complexes.

In ZnO:Cu NCs the XRD peak intensity increases versus etching durations (**Figure 19**) due to thickness increasing of the ZnO Cu NC layers. Simultaneously, the new XRD peak (2θ = 43.2963°) related to the diffraction from (111) crystal planes in metallic Cu nanoparticles with a cubic crystal lattice [73] has been revealed (**Table 5**, **Figure 19**).

6.2. Comparative PL study of ZnO and ZnO Cu NCs

PL spectra of ZnO and ZnO Cu NCs obtained at different etching times (3 and 6 min) and measured at 10 K are presented in **Figure 20(a)** and **(b)**. PL spectra are complex and include two wide PL bands well known in ZnO:NBE emission in the spectral range 2.80–3.37 eV [34] and defect-related emission in the range 1.70–2.80 eV [37–39]. The intensity of NBE luminescence rises versus anodization time owing to enlarging the thickness of ZnO NC layers (**Figure 20a** and **b**).

Simultaneously, the NBE band shifts to lower energy in PL spectra (**Figure 20a** and **b**) that is caused by decreasing the NC sizes, compressive strains, and the energy band gap of ZnO NCs [26].

The variation of Cu concentrations in ZnO:Cu NCs influent mainly on the intensity and shape of defect-related PL bands in the range 1.7–2.8 eV. PL band intensity increases when the Cu concentration approaches to 2.28 at% and then decreases at higher Cu contents (**Figure 20a** and **b**). At high Cu concentration, the new PL band centered at 2.61–2.70 eV at 10 K has been detected in PL spectra of ZnO Cu NCs (**Figure 20b**, curve 2).

To make the conclusion concerning the light-emitting mechanisms of visible PL bands in ZnO:Cu NCs, PL spectra have been studied in the range of 10–300 K (**Figure 21**).

Normalized PL spectra of ZnO and ZnO:Cu NCs for the visible spectral range measured at different temperatures are presented in **Figure 22(a)** and **(b)**. It is clear that four PL bands (A, B, C, D) have composed PL spectra in the orange-yellow-green-blue ranges of ZnO Cu NCs, which are characterized by different kinetics of PL intensity thermal decays.
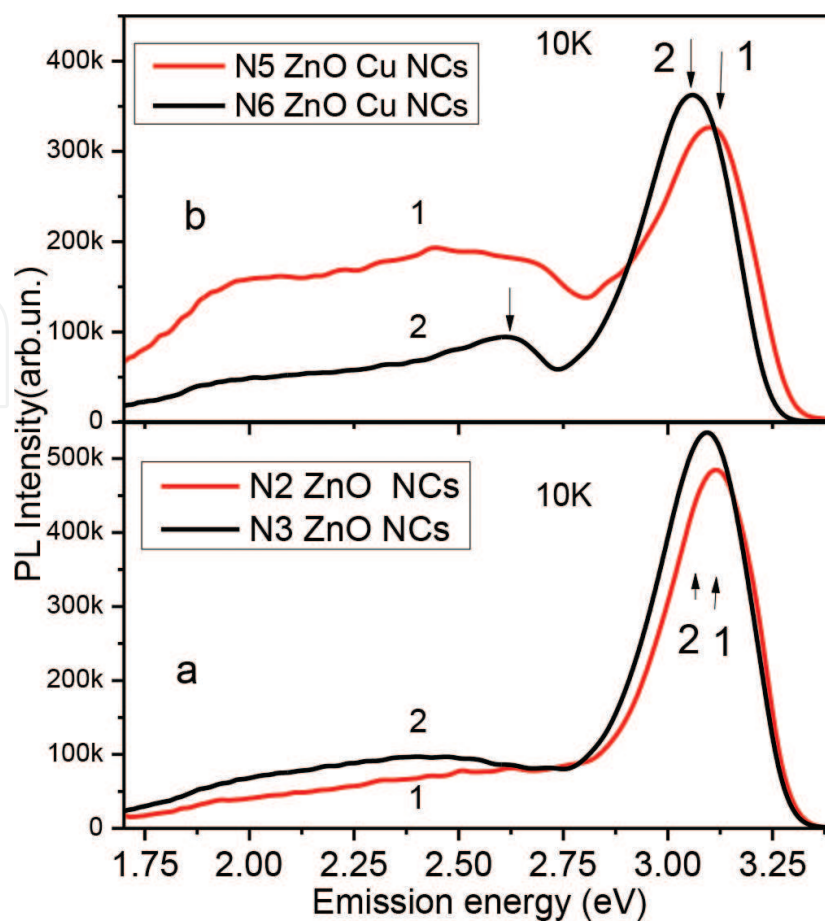
Figure 20. PL spectra of N2 (curve 1) and N3 (curve 2) ZnO NCs (a) and N5 (curve 1) and N6 (curve 2) ZnO Cu NCs (b).

The deconvolution procedure was applied to PL spectra of **Figure 22(a)** and **(b)** that permits to obtain three- and four-elementary PL bands in ZnO and ZnO Cu NCs, respectively, peaked at 10 K: 1.95–2.00 eV(A), 2.15–2.23 eV(B), 2.43–2.50 eV(C), and 2.61–2.69 eV(D).

The PL intensity of bands A, B, and C decreases faster (N6) versus etching duration in comparison with the PL intensity of band D (**Figure 20b**, curve 2). The variation of integrated PL intensities of all PL bands versus temperatures in ZnO and ZnO Cu NCs is presented in **Figure 23(a)** and **(b)**. The band D intensity decreases at low temperatures (starting from 70 K). PL thermal decays of the bands A, B, and C are similar in ZnO and ZnO Cu NCs. PL intensities of bands (A, B, C) fall down slowly in the range 10–100 K, and only at higher temperatures (100–300 K) their PL thermal decays become faster.

To estimate the activation energies of PL thermal decay in different temperature ranges, the Arrhenius plots have been designed (**Figure 24**). At low temperatures, the activation energies of PL intensity decays are estimated as: 9 meV in ZnO or 16 meV in ZnO Cu NCs. These small activation energies of PL decay are related to the thermal activation of some nonradiative recombination centers (NRC). At higher temperatures PL intensities of A, B, and C bands decay with activation energies: 44meV (A) and 35 meV (B and C) in ZnO NCs (**Figure 24a**) as well as 37 meV (A) and 27 meV (B and C) in ZnO Cu NCs (**Figure 24b**). The PL band D intensity decreases with the activation energy of 20 meV (**Figure 24b**, curve 4).
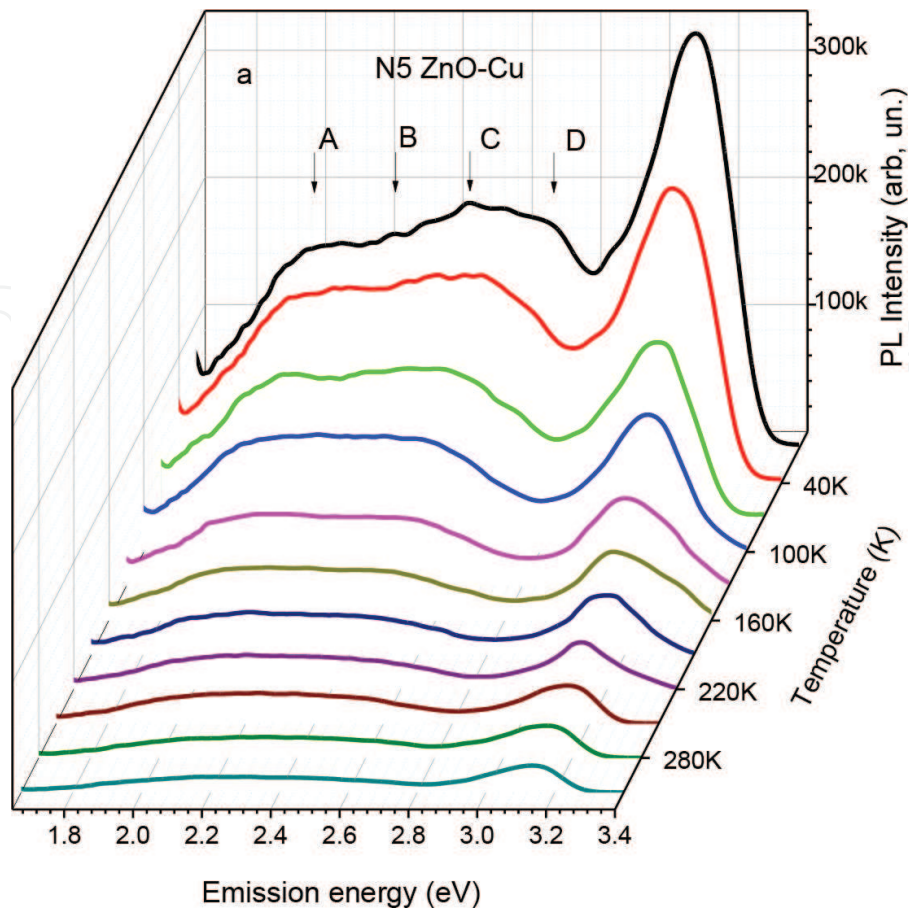
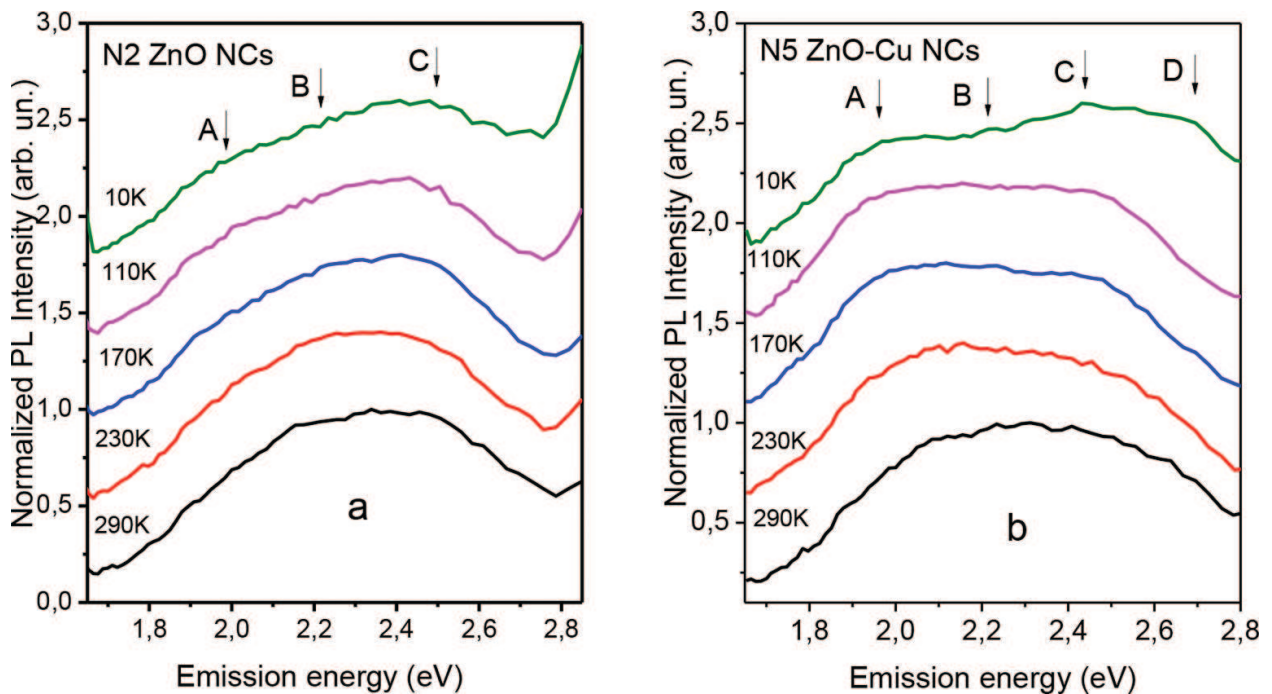**Figure 21.** PL spectra of ZnO:Cu NCs measured in the range 10–300K.

Figure 22. Normalized PL spectra in the range of defect-related PL bands for ZnO NCs (a) and ZnO Cu NCs (b).
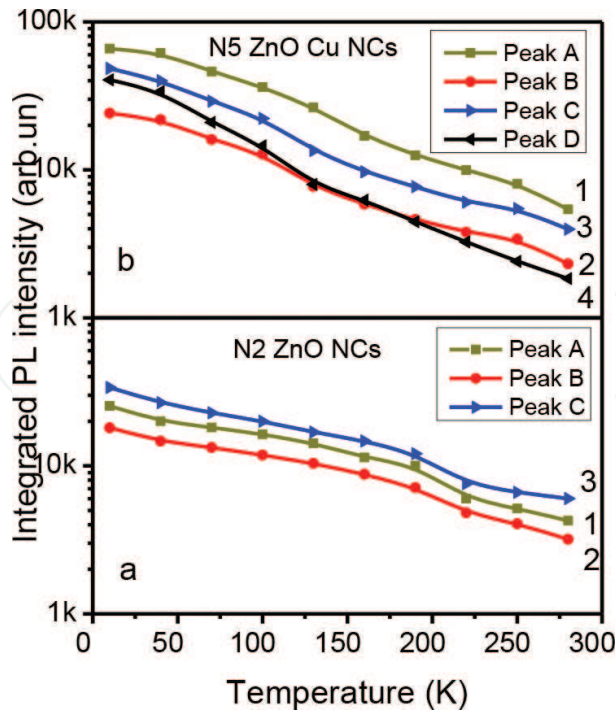
Figure 23. Thermal dependences of integrated PL intensities in ZnO (a) and ZnO Cu NCs (b) [66].
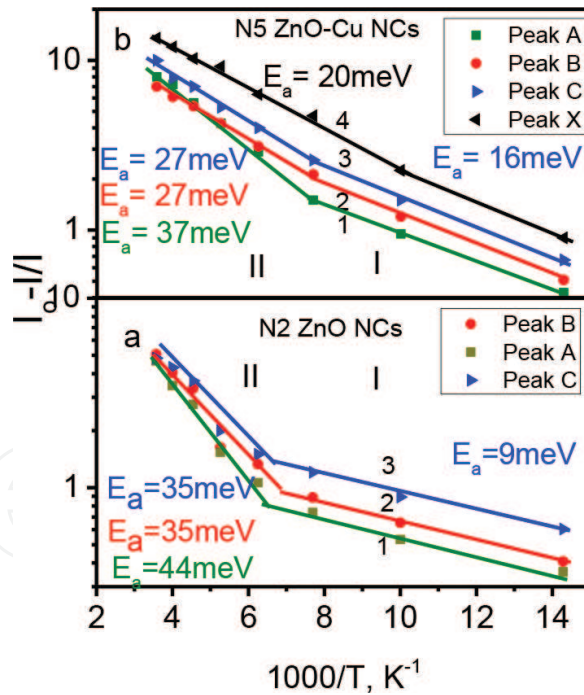

Figure 24. Arrhenius plots obtained for different PL bands for ZnO (a) and ZnO Cu NCs (b) [67].

6.3. Orange-yellow-green PL bands

The orange PL band (1.95–2.05 eV) in ZnO was assigned to oxygen interstitials, O_i (2.02 eV) [40], to shallow donor-deep acceptor pairs [11], or to hydroxyl groups (2.10 eV) [41]. The yellow band (2.15–2.23 eV) in undoped and doped (with N or Ga) ZnO layers [11, 74] was

attributed to the electron transitions from shallow donors to deep acceptors with an energy level of 0.7 eV above the valence band, connected with the zinc vacancy, V_{Zn}, or V_{Zn}-shallow donor complex [11]. The green PL band (2.43–2.50 eV) is complex and includes five PL bands connected with different defects in undoped ZnO NCs [75–78]. The types of corresponding defects and optical transitions are not clear yet.

The ZnO and ZnO:Cu NC layers were annealed at 400°C in air that is the O- and N-rich condition. The defects favored for this condition are V_{Zn}, O_i, and O_{Zn} [79] that act as deep acceptors in ZnO [79]. However, the probability of forming O_{Zn} defects is low due to the high value of its formation energy in ZnO. The PL intensity of 2.40–2.50 eV band increases with NC size decreasing and surface-to-volume ratio rising [26], which permits to attribute the green radiative centers to native defects (zinc vacancy or surface defects) in ZnO NCs (**Figure 20a**).

Cu doping with the concentration ≤2.28 at% stimulates significantly the intensity of orange-yellow-green PL bands in ZnO:Cu NCs (**Figure 20b** and **Table 4**). Simultaneously, the XRD study has detected a high angle shift of all XRD peaks in ZnO Cu NCs owing to, apparently, the substitution of Zn^{+2} ions by Cu^{+2} ions in ZnO. Thus, the radiative centers connected with structureless green PL band (2.43–2.50 eV) in ZnO:Cu NCs can be attributed to Cu_{Zn}^{+2} defects [64, 65].

The high PL intensity of green band is detected together with the high intensities of orange and yellow PL bands in the ZnO Cu NCs (**Figure 20b**). It can be supposed that the process of Zn^{+2} ion substitution by Cu^{+2} ions at the thermal treatment (400°C) is accompanied by appearing other native acceptors: zinc vacancies, oxygen interstitials, or their complexes. Zinc vacancies, V_{Zn}, are the deep acceptors with the transition energy levels $E^{(0/-)} = 0.18$ eV and $E^{(-/2-)} = 0.87$ eV above the valence band according to the calculations reported in [79]. Oxygen interstitials are characterized by deep acceptor transition levels $E^{(0/-)} = 0.72$ and $E^{(-/2-)} = 1.59$ eV above the valence band [79]. Cu atoms act as deep acceptors in ZnO as well [80]. Thus, all these deep acceptors can be responsible for the stimulation of orange-yellow-green PL bands in ZnO:Cu NCs.

Small activation energies of emission thermal decays (**Figure 24**) for bands (A, B, C) permit to attribute the corresponding centers to the shallow donor-deep acceptor pars (DAPs). Note that PL thermal decays of B and C bands are characterized by the same activation energies owing to, apparently, the formation of corresponding DAPs from the same shallow donors, for example, Zn_i, and different deep acceptors.

Note that the defect concentration in ZnO:Cu NCs is higher than its value in ZnO NCs. Defect concentration increasing leads to the stimulation of the PL intensities of A, B, and C bands. Simultaneously, the activation energies of PL decays decrease in ZnO Cu NCs that is a result of distance decreasing between donors and acceptors in DAPs. The last effect provokes attractive interaction increasing in DAPs and, as a result, the shift of donor and acceptor energy levels closer to the conduction (valence) bands. In this case, the PL thermal decays in ZnO:Cu NCs are characterized by smaller activation energies that actually has been revealed: 37 meV (A) and 27 meV (B and C) (**Figure 24**).

The energy position of $Zn_i^{+1/0}$ donor levels was estimated early as 50 meV [81]. A shallow donor with ionization energy of 30 meV was detected at high-energy electron irradiation experiments [82]. The authors suggested that these shallow donors owe to Zn-sublattice

defects: Zn interstitialses or Zn-interstitial-related complex [83]. In addition, under the N-rich ambient condition the shallow donors, Zn_i–N_O, can be obtained as it was supposed in [84]. Thus, it can be assumed that in ZnO NCs the orange (A), yellow (B), and green (C) emissions are related to DAPs, which include the deep acceptors, such as oxygen interstitials and zinc vacancies, and shallow donors, like zinc interstitials or their complexes. In ZnO Cu NCs the substitutional Cu_{Zn} atoms form the DAPs with shallow donors that are responsible on the structureless green PL band.

6.4. Blue PL band

The blue PL band D (2.61–2.70 eV) appears in PL spectra of ZnO:Cu NCs (sample N6, **Figure 20b**) at higher Cu contents (≥2.28 at%). Simultaneously, the intensities of other PL bands decrease (**Table 4**) and the band D dominates in the PL spectrum (**Figure 20b**, curve 2). At higher Cu concentrations in ZnO:Cu NCs, the nonradiative recombination centers (NRC), probably, appear that provokes decreasing the PL intensity of the bands (A, B, C). At the same time, the D band intensity decreases slowly that testifies on concentration increasing of D band emitting defects. In this case, a low angle shift of XRD peaks has been revealed at XRD study. This fact testifies on increasing the lattice parameters and interplanar distances owing to the formation of some Cu-related complexes in the ZnO matrix. Cu-complex defects can be attributed to $[Cu_{Zn} Zn_i]_x$ complexes proposed in [65].

7. Plasmon-related effects in ZnO Cu NC films with metallic Cu nanoparticles

The purpose of this part deals with the study of another effect related to Cu doping of the ZnO NCs. In the earlier mentioned papers [11, 58–63], the ZnO NCs were doped by Cu in low concentrations, when Cu atoms substituted Zn atoms in the ZnO crystal lattice. However, the method of Zn etching technology with thermal treatment permits to prepare ZnO:Cu NCs with metallic Cu nanoparticles located at the ZnO NC surface (**Figure 19**, **Table 5**). In this ZnO:Cu films, as expected, it is possible to generate plasmon by light in Cu nanoparticles that permit to study its impact on optical properties [80].

At first, the XRD (**Figure 19**) and EDS (**Figure 25**) methods have been used for the confirmation that Cu atoms and Cu nanoparticles exist in ZnO Cu NC films (**Table 6**).

Figure 25(b) clearly demonstrates the Cu_K line in the high resolution insertion for ZnO:Cu NCs. The EDS analysis and estimated element concentrations are presented in **Table 6**.

XRD comparative investigations of ZnO and ZnO Cu NCs have been presented early in **Figures 18** and **19** and analyzed in Section 6. In addition to the above discussed Cu peak at 2 theta equal to 43.2963° (**Figure 19**), which corresponds to the diffraction from the (111) crystal planes in the cubic crystal lattice of metallic Cu nanoparticles [73], the second Cu (200) peak at the 2 theta equaling to 50.4308° has been revealed in ZnO Cu NCs as well (**Figure 26a** and **b**) [85].
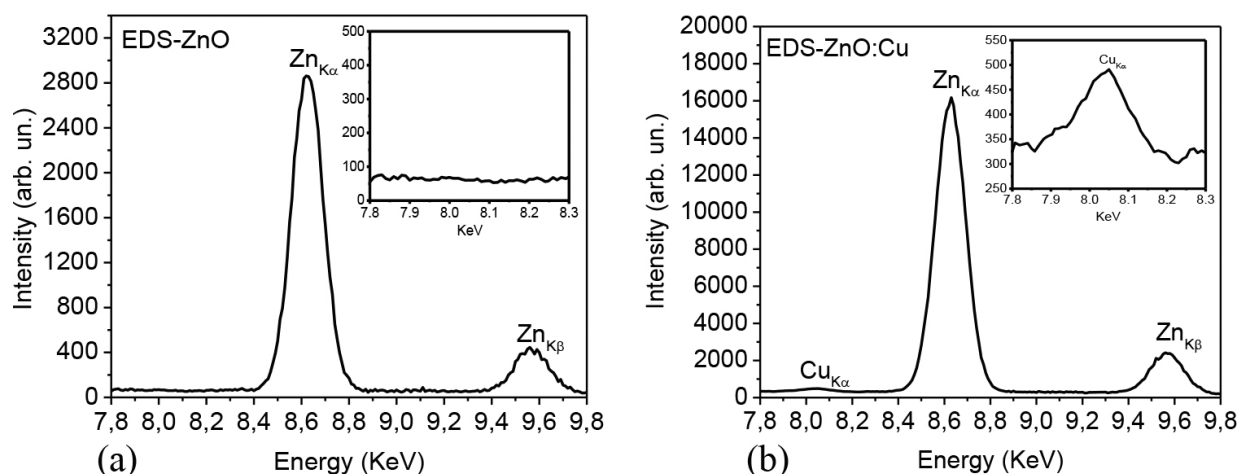
Figure 25. EDS spectra of N3-ZnO (a) and N6-ZnO Cu (b) NC samples obtained at an anodization time 6 min after thermal annealing [85]. The insertions present the high resolution EDS spectra in the range 7.8-8.3 keV for ZnO (a) and ZnO:Cu (b) NCs.

In ZnO:Cu NCs obtained with the etching time of 6 min, the concentration of Cu NCs enlarges, which manifests itself by increasing the intensity of the Cu (111) and Cu (200) XRD peaks (**Figures 19b** and **26b**). The oxidation of Cu nanoparticles can be realized, partially as well, at annealing in ambient air. The small peculiarities in XRD diagrams (**Figure 19**) for the sample M6 in the range 38–40° can be related to the CuO or Cu_2O phases.

7.1. Raman scattering study

Raman peaks at 331, 379, 437, and 572–575 cm^{-1} have been detected in Raman scattering spectra measured in the 100–650 cm^{-1} range in ZnO and ZnO:Cu NCs (**Figure 27**). The nature of these Raman peaks has been discussed in Section 3.2. The increase in etching time leads to the enlargement of Raman peak intensities owing to the growth of ZnO NC volume and varying the geometry of Raman scattering measurement in small ZnO NC films (**Figure 27**). The intensity of all Raman peaks in ZnO Cu NCs is threefold higher than its value in ZnO NCs (**Figure 27a** and **b**). The studied NCs are characterized by the identical crystal structure and NC sizes (**Table 4**). The difference in the Raman scattering intensity can be attributed to the surface-enhanced Raman scattering (SERS) effect in ZnO Cu NCs [72].

Element	wt%	at%
O_K	19.87	50.29
Cu_K	3.58	2.28
Zn_K	76.55	47.42
Sum	100	100

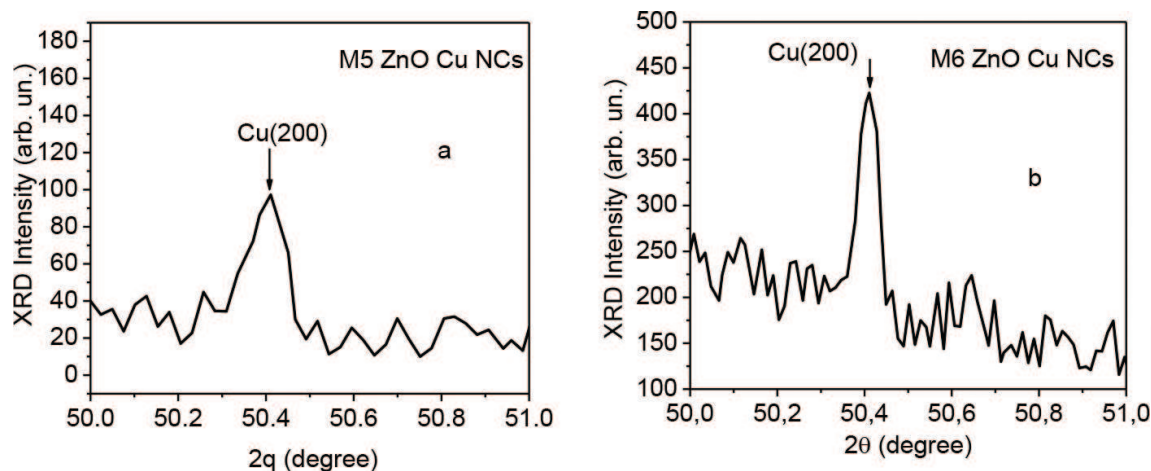**Table 6.** Analysis of K-lines in EDS results for N5 ZnO Cu NCs.

Figure 26. XRD results for the ZnO Cu NCs obtained at an anodization times of 3 min (a) and 6 min (b) after thermal annealing in the XRD range 50–51° [85].

The light-enhanced electric field and the SERS effect are attributed to the plasmon resonance at the material interface with metallic nanoparticles. In the studied case, apparently, the excitation light used at Raman scattering study stimulates the plasmon generation in metallic Cu nanoparticles at the surface of ZnO:Cu NCs with corresponding wavelength for plasmon-polariton resonance that is needed for SERS effect.

7.2. ZnO emission study

PL spectra of ZnO and ZnO Cu NCs are presented in **Figure 28** for the comparison. The PL intensity of defect-related PL bands (2.08 and 2.50 eV) increases, in comparison with the NBE emission intensity, when the NC size falls down in ZnO and ZnO Cu NCs together with the surface-to-volume ratio rising (**Figure 28**, **Table 4**). It is known that 2.02–2.08 eV PL band
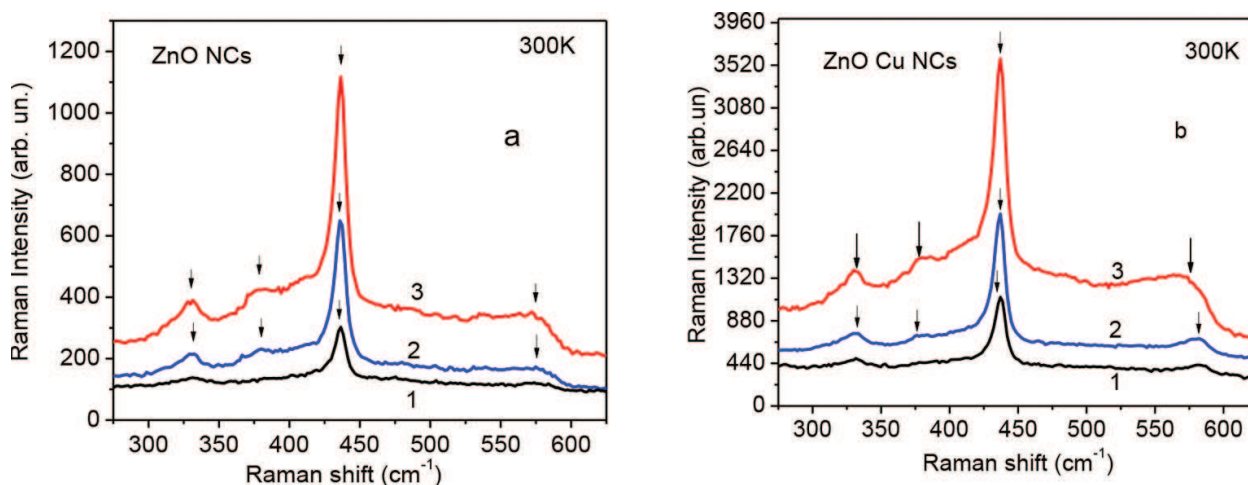

Figure 27. Raman scattering spectra of thermal annealed ZnO NCs (a) and ZnO Cu NCs (b) obtained at the etching times: 1 (1), 3 (2), and 6 min (3) [85].
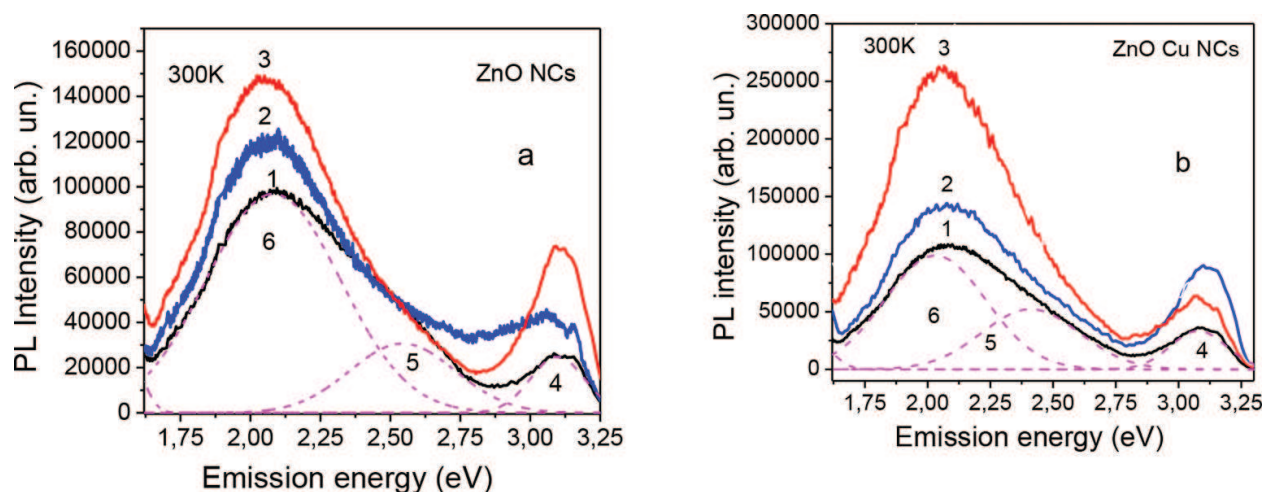
Figure 28. PL spectra of ZnO NCs (a) and ZnO Cu NCs (b) obtained at the anodization durations of 1 (1), 3 (2), and 6 min (3). Dashed curves represent the deconvolution of experimental PL spectrum on the elementary PL bands (curves 4, 5, 6) [85].

increased significantly its intensity after oxidation at annealing in ambient air [21, 22] that is accompanied by the oxygen interstitial content enlargement in ZnO. The detection of identical orange emission peaks in ZnO and ZnO Cu NCs permits to attribute the PL band (2.08 eV) to radiative defects included the oxygen interstitials.

The influence of metallic Cu nanoparticles on the PL band intensities in PL spectra of ZnO:Cu NCs is different significantly.

The influence of Cu nanoparticles on the intensities of PL bands in ZnO NCs is different. **Figure 28** shows that the PL intensity of defect-related PL bands is higher by twofold in ZnO Cu NCs than it value in ZnO NCs. This fact can be assigned to the plasmon-enhancing recombination via these defects [1]. However, NBE emission in ZnO Cu NCs is less effective in comparison with ZnO NCs (**Figure 28**). The last effect can be explained by the destruction of excitons by locally enhanced electric field in Cu nanoparticles at the ZnO Cu NC surface and due to this diminish the exciton-related emission.

8. Conclusion

The morphology, crystal structure, Raman scattering, and multicolor emission have been comparatively studied in ZnO and ZnO:Cu NCs. XRD study confirms the wurtzite structure of ZnO NCs obtained by electrochemical method. The PL intensity enhancement of exciton emission is detected in NCs with the size of 67–170 nm and attributed to the week quantum confinement and exciton light coupling with the formation of polaritons. It is shown that metallic Cu nanoparticles on the surface of ZnO:Cu NCs stimulate the SERS effect and PL intensity rising the visible PL bands owing to, apparently, the plasmon generation in Cu NCs. Simultaneously, NBE emission decreases in ZnO:Cu NCs due to the exciton destruction by plasmon-enhanced electric field.

Acknowledgements

Author details

Tetyana V. Torchynska[1]* and Brahim El Filali[2]

*Address all correspondence to: ttorch@esfm.ipn.mx

1 Instituto Politecnico Nacional, ESFM, Mexico City, Mexico

2 Instituto Politecnico Nacional, UPIITA, Mexico City, Mexico

References

[1] T.V. Torchynska, Nanocrystals and Quantum Dots. Some Physical Aspects, in "*Nanocrystals and Quantum Dots of Group IV Semiconductors*", Eds: T.V. Torchynska and Y. Vorobiev, American Scientific Publisher, Stevenson Ranch, CA, pp. 1–42 (2010).

[2] L. Schacht Hernandez, T.V. Torchynska, J.A. Hernandez, G. Polupan, Y. Goldstein, A. Many, et al., Microelectronic Eng. 66, 83 (2003).

[3] T.V. Torchinskaya, N.E. Korsunskaya, B. Dzumaev, B.M. Bulakh, O.D. Smiyan, A.L. Kapitanchuk, S.O. Antonov, Semiconductors 30, 792 (1996).

[4] S.J. Pearton, D.P. Norton, K. Ip, Y.W. Heo, T. Steiner, Prog. Mater. Sci. 50, 293 (2005).

[5] N.H. Alvi, S. Hussain, O. Nur, M. Willander, Scripta Mater. 64, 697 (2011).

[6] M.H. Huang, S. Mao, H. Feick, Science 292, 1897 (2001).

[7] Y.B. Li, Y. Bando, D. Golberg, Appl. Phys. Lett. 84, 3603 (2004).

[8] W.I. Park, J.S. Kim, G.C. Yi, M.H. Bae, H.J. Lee, Appl. Phys. Lett. 85, 5052 (2004).

[9] K. Keis, E. Magnusson, H. Lindstrom, Sol. Energy Mater. Sol. Cells 73, 51 (2002).

[10] D. Gruber, F. Kraus, J. Muller, Sens. Actuators B 92, 81 (2003).

[11] M.A. Reshchikov, H. Morkoc, B. Nemeth, J. Nause, J. Xie, B. Hertog, A. Osinsky, Physica B. Condensed Matter 358, 401 (2007).

[12] F. Benharrats, K. Zitouni, A. Kadri, B. Gil, Superlat. Microstruct. 47, 592 (2010).

[13] T. Saidani, M. Zaabat, M.S. Aida, A.B. Aboud, S. Benzitouni, A. Boudine, Superlat. Microstruct. 75, 47 (2014).

[14] S.S. Shinde, C.H. Bhosale, K.Y. Rajpure, J. Photoch. Photobiol. B 120, 1 (2013).

[15] S. Xiang-Bing, F. Lin, J. Xian-Wei, Chin. Phys. B 20, 067804 (2011).

[16] N. Kumar, R. Kaur, R.M. Mehra, J. Lumines. 126, 784 (2007).

[17] X. Zhou, S. Gu, Z. Wu, S. Zhu, J. Ye, S. Liu, R. Zhang, Y. Shi, Y. Zheng, Appl. Surf. Sci. 253, 2226 (2006).

[18] L. Esaki, C.L. Chang, Thin Solid Films 36, 285 (1976).

[19] A.V. Singh, R.M. Mehra, A. Yoshida, A. Wakhara, J. Appl. Phys. 90, 5661 (2001).

[20] W. Tang, D.C. Cameron, Thin Solid Films 238, 83 (1994).

[21] A.I. Diaz Cano, B. El Filali, T.V. Torchynska, Physica E 51, 24 (2013).

[22] A.I. Diaz Cano, B. El Falali, T.V. Torchynska, J. Phys. Chem. Solids 74, 431 (2013).

[23] N. Korsunska, L. Khomenkova, M.K. Sheinkman, T. Stara, V. Yuhimchuk, T.V. Torchynska, A. Vivas Hernandez, J. Lumines. 115, 117 (2005).

[24] T.V. Torchynska, J. Palacios Gomez, G.P. Polupan, F.G. Becerril Espinoza, A. Garcia Borquez, N.E. Korsunskaya, L.Y. Khomenkova, Appl. Surf. Science 167, 197 (2000).

[25] A. Diaz Cano, S. Jiménez Sandoval, Y. Vorobiev, F. Rodriguez Melgarejo, T.V. Torchynska, Nanotechnology 21, 134016 (2010).

[26] T.V. Torchynska, B. El Filali, J. Lumines. 149, 54 (2014).

[27] PDF2 XRD database, Reference code: 00-004-0831 (Zn) and 00-036-1451 (ZnO).

[28] N. Ashkenov, B.N. Mbenkum, C. Bundesmann, V. Riede, M. Lorenz, D. Spemann, E.M. Kaidashev, A. Kasic, M. Schubert, M. Grundmann, G. Wagner, H. Neumann, V. Darakchieva, H. Arwin, B. Monemar, J. Appl. Phys. 93, 126 (2003).

[29] J.F. Scott, Phys. Rev. B 2, 1209 (1970).

[30] A.V. Fedorov, A.V. Baranov, K. Inoue, Phys. Rev. B 56, 7491 (1997).

[31] G. Polupana, T.V. Torchynska, Thin Solid Films 518, S208 (2010).

[32] V.A. Coleman, C. Jagadish, Basic Properties and Applications of ZnO, in "*Zinc Oxide Bulk, Thin Films and Nanostructures*", Eds: C. Jagadish and S. Pearton, Elsevier, Amsterdam, pp. 2–20 (2006).

[33] S. Ghoopum, N. Hongsith, P. Mangkorntong, Physica E 39, 53 (2007).

[34] A.B. Djurišic, A.M. Ng, X.Y. Chen, Prog. Quantum Electron. 34, 191 (2010).

[35] T. Voss, C. Bekeny, L. Wischmeier, H. Gafsi, S. Borner, W. Schade, A.C. Mofor, A. Bakin, A. Waag, Appl. Phys. Lett. 89, 182107 (2006).

[36] M.K. Patra, K. Manzoor, M. Manoth, N. Kumar, J. Lumin. 128, 267 (2008).

[37] D.H. Zhang, Z.Y. Xue, Q.P. Wang, J. Phys. D Appl. Phys. 35, 2837 (2002).

[38] N.Y. Garces, L. Wang, N.C. Giles, G. Cantwell, Appl. Phys. Lett. 81, 622 (2002).

[39] A.B. Djurišic, W.C.H. Choy, V.A.L. Roy, Y.H. Leung, C.Y. Kwong, K.W. Cheah, T.K. Gundu Rao, W.K. Chan, H.F. Lui, C. Surya, Adv. Funct. Mater. 14, 856 (2004).

[40] X. Liu, X. Wu, H. Cao, R.P.H. Chang, J. Appl. Phys. 95, 3141 (2004).

[41] J. Qiu, X. Li, W. He, S.-J. Park, H.-K. Kim, Y.-H. Hwang, J.-H. Lee, Y.-D. Kim, Nanotechnology 20, 155603 (2009).

[42] R.B.M. Cross, M.M. De Souza, E.S. Narayanan, Nanotechnology 16, 2188 (2005).

[43] S. Xiang-Bing, F. Lin, J. Xian-Wei, Chin. Phys. B 20, 067804 (2011).

[44] N. Kumar, R. Kaur, R.M. Mehra, J. Lumines. 126, 784 (2007).

[45] X. Zhou, S. Gu, Z. Wu, S. Zhu, J. Ye, S. Liu, R. Zhang, Y. Shi, Y. Zheng, Appl. Surf. Sci. 253, 2226 (2006).

[46] C. Klingshirn, Phys. Status Solidi (a) 71, 547 (1975).

[47] T.V. Torchynska, A.I. Diaz Cano, J.A. Yescas Hernandez, Y. Shcherbyna, J. Nanoparticle Res. 14, 19 (2011).

[48] B. Gil, A.V. Kavokin, Appl. Phys. Lett. 81, 748 (2002).

[49] S.V. Gupalov, E.L. Ivchenko, A.V. Kavokin, J. Exp. Theor. Phys. 86, 388 (1998).

[50] E.I. Rashba, G.E. Gurgenishvili, Sov. Phys. Solid State 4, 759 (1962).

[51] W.-T. Hsu, K.-F. Lin, W.-F. Hsieha, Appl. Phys. Lett. 91, 181913 (2007).

[52] D.M. Bagnall, Y.F. Chen, M.Y. Shen, T. Goto, Appl. Phys. Lett. 73, 1038 (1998).

[53] T. Makino, C.H. Chia, N.T. Tuan, Y. Segawa, M. Kawasaki, A. Ohtomo, K.Tamura, H. Koinuma, Appl. Phys. Lett. 76, 3549 (2000).

[54] C.H. Ahn, S.K. Mohanta, H.K. Cho, Appl. Phys. Lett. 94, 261904 (2009).

[55] M.H. Mamat, M.Z. Sahdan, Z. Khusaimi, A. Zain Ahmed, S. Abdullah, M. Rusop, Optical Mater. 32, 696 (2010).

[56] S.A. Ansari, A. Nisar, B. Fatma, W. Khan, A.H. Naqvi, Mater. Sci. Eng. 177, 428 (2012).

[57] M. ElHilo, A. Dakhel, A. Ali-Mohamed, Magnet. Magn. Mater. 321, 2279 (2009).

[58] S. Singhal, J. Kaur, T.S. Namgyal, R. Sharma, Physica B. 407, 1223 (2012).

[59] H. Liu, J. Yang, Z. Hua, Y. Zhang, L. Yang, Appl. Surf. Sci. 256, 4162 (2010).

[60] E. Velázquez, L.T. Torchynska, J.L. Casas, Espinola Physica B 453, 111 (2014).

[61] Y. Zhao, M. Zhou, Z. Li, et al., J. Lumines. 131, 1900 (2011).

[62] X.B. Wang, C. Song, K.W. Geng, et al., Appl. Surf. Sci. 253, 6905 (2007).

[63] Q.A. Drmosh, S.G. Rao, Z.H. Yamani, et al., Appl. Surf. Sci. 270, 104 (2013).

[64] R. Dingle, Phys. Rev. Lett. 23, 579 (1969).

[65] N.Y. Garces, L. Wang, L. Bai, N.C. Giles, L.E. Halliburton, G. Cantwell, Appl. Phys. Lett. 81, 622 (2002).

[66] T.V. Torchynska, B. El Filali, I.C. Ballardo Rodríguez, Physica E 75, 156 (2016).

[67] T. V. Torchynska, B. El Filali, L. Shcherbyna, Phys. Stat. Sol. (c) 13, 594 (2016).

[68] B. Kulyk, B. Sahraoui, V. Figà, B. Turko, J. Alloys Compounds. 481, 819 (2009).

[69] M. Ligang, M. Shuyi, H. Chen, X. Ai, X. Huang, Appl. Surf. Sci. 257, 10036 (2011).

[70] L. Chowa, O. Lupana, G. Chaia, H. Khallaf, L.K. Ono, B. Roldan Cuenya, I.M. Tiginyanu, V.V. Ursaki, V. Sontea, A. Schulte, Sensors Actuators A 189, 399 (2013).

[71] Y. Yan, M.M. Al-Jassim, S.H. Wei, Appl. Phys. Lett. 89, 181912 (2006).

[72] X. Peng, J. Xu, X. Zang, et al., J. Lumines. 128, 297 (2008).

[73] PDF2 XRD data base, Reference code: 00-004-0836.

[74] H. Morkos, U. Ozgur, *Zinc Oxide. Fundamentals, Materials and Device Technology*, Wiley-VCH, Weinheim, 469 p (2009).

[75] R.B. Lauer, J. Phys. Chem. Solids 34, 249 (1973).

[76] D.C. Reynolds, D.C. Look, B. Jogai, H. Morkoc, Sol. St. Commun. 101, 643 (1997).

[77] D.C. Reynolds, D.C. Look, B. Jogai, J.E. Van Nostrand, R. Jones, J. Jenny, Solid State Commun. 106, 701 (1998).

[78] B. Lin, Z. Fu, Y. Jia, Appl. Phys. Lett. 79, 943 (2001).

[79] A. Janotti, C.G. Van de Walle, Rep. Prog. Phys. 72, 126501 (2009).

[80] F.J. Garsia Rodriguez, et al., J. Raman Spectrosc. 29, 763 (1998).

[81] F.A. Kröger, *The Chemistry of Imperfect Crystals*. 2nd Edn, North Holland, Amsterdam, p. 73 (1974).

[82] D.C. Look, J.W. Hemsky, J.R. Sizelove, Phys. Rev. Lett. 82, 2552 (1999).

[83] A. Janotti, C.G. Van de Walle, Appl. Phys. Lett. 87, 122102 (2005).

[84] D.C. Look, G.C. Farlow, P. Reunchan, S. Limpijumnong, S.B. Zhang, K. Nordlund, Phys. Rev. Lett. 95, 225502 (2005).

[85] B. El Filali, T.V. Torchynska, A.I. Diaz Cano, J. Lumines. 161, 25 (2015).